ORIGINAL PAPER

Design of a metastructure for vibration isolation with quasi-zero-stiffness characteristics using bistable curved beam

Srajan Dalela · **P. S. Balaji** · **D. P. Jena**

Abstract This work designs and analyzes a metastructure-based vibration isolation model to improve small-scale equipment's isolation effectiveness under low-frequency excitations. The feature of the proposed model is the high static and low dynamic stiffness characteristics, also called quasi-zero-stiffness (QZS), possessed by the metastructure under vertical load. The metastructure consists of four parallelly arranged unit cells, and the QZS property is realized in each unit cell by the snap-through behavior of the cosine beam system and the bending-dominated behavior of semicircular arches. The static characteristics of the metastructure are studied analytically and numerically and validated with experimental results. Based on the static analysis results, the dynamic equation of the proposed metastructure is set up in the form of Duffing's equation. The harmonic balance method is used to calculate the frequency response and motion transmissibility of the metastructure at steady state for a harmonic load. The time and frequency responses under the sinusoidal base excitation are examined analytically and numerically, and their results are compared. The simulation results revealed that the proposed QZS metastructure obtains lower transmissibility and wider effective isolation range compared to the equivalent linear model. The parametric study shows that in the low-frequency excitation region, the motion transmissibility increases with decreasing damping ratio, whereas for the effective isolation range, the motion transmissibility increases with increasing damping ratio. Finally, stability analysis is performed to study the unstable region in the frequency response curve. The parametric study indicates that the unstable region reduces with the increase in damping ratio and remains unaffected with varying excitation amplitude.

List of symbols

A	Amplitude
b_1	Depth of cosine beam
b_2	Depth of semicircular arch
dB	Decibel
E_1	Young's modulus of cosine beam
E_2	Young's modulus of semicircular arch
FR	Frequency response
f_{app}	Fifth-order approximation of dimensionless reaction force
f_{QZS}	Dimensionless equivalent reaction force
F_h	Reaction force exerted by cosine beam system

S. Dalela · P. S. Balaji (✉)
Department of Mechanical Engineering, National Institute
of Technology, Rourkela 769008, India
e-mail: aerobala@gmail.com; psbalaji@nitrkl.ac.in

D. P. Jena
Department of Industrial Design, National Institute of
Technology, Rourkela 769008, India

F_v	Reaction force exerted by semicircular arch
F_{NSM}	Restoring force for the negative stiffness mechanism
F_{QZS}	Equivalent reaction force
h	Height of cosine beam
Hz	Hertz
HB	Harmonic balance
HSLDS	High-static–low-dynamic stiffness
I_1	Moment of Inertia of cosine beam
I_2	Moment of inertia of semicircular arch
k_{app}	Fifth-order approximation of dimensionless stiffness
k_c	Vertical stiffness of cosine beam system
k_h	Equivalent stiffness of cosine beam system
k_v	Equivalent stiffness of semicircular arch
k_s	Vertical stiffness of semicircular arch
K_{eq}	Equivalent stiffness of metastructure
l_1	Length of cosine beam
l_2	Length of semicircular arch
L_0	Original length of cosine beam without any deformation
L_1	Projected length of cosine beam on horizontal plane
L_{sd}	Length of low-stiffness–displacement range
m	Mass of isolated object
m	Number of rows of unit cell
mm	Millimeter
n	Number of columns of unit cell
NSM	Negative stiffness mechanism
Q	Height-to-thickness ratio of cosine beam
QZS	Quasi-zero stiffness
R	Radius of semicircular arch
RMS	Root mean square
t	Time
T	Transmissibility
TPU	Thermoplastic polyurethane
t_1	Thickness of cosine beam
t_2	Thickness of semicircular arch
x	Dimensionless vertical displacement of unit cell from static equilibrium position
X	Vertical displacement of unit cell form static equilibrium position
y	Dimensionless relative displacement between base and isolated mass
Y	Relative displacement between base and isolated mass
z	Amplitude of wave excitation

| z_0 | Dimensionless excitation acceleration amplitude |
| $\ddot{Z}$ | Excitation acceleration amplitude applied at the base |

Greek letters

θ	Angle between cosine beam and horizontal plane
μ	Stiffness ratio
γ	Geometrical parameter
α	Coefficient of third-order dimensionless displacement
δ	Coefficient of fifth-order dimensionless displacement
us	Unstable
c	Damping coefficient
ω_n	Natural frequency of the system
ω	Applied excitation frequency
ξ	Damping ratio
τ	Dimensionless time
ϕ	Phase response
Ω	Frequency ratio

Subscripts

u	Jump-up
d	Jump-down
p	Peak
us	Unstable
h	Horizontal
v	Vertical
app	Approximation
eq	Equivalent

Superscripts

| • | Time derivative |
| ′ | Dimensionless time derivative |

1 Introduction

Vibration is a common phenomenon in the natural world that can lead to human discomfort, degrading machine performances, catastrophic failures, and many more. A wide amount of research has been carried out to reduce the impact of vibration to be transmitted: either from payload to host structure or from host structure to payload. A passive vibration isolation system is mostly used to attenuate unwanted waves because of their cost-effectiveness and relia-bility [1]. The earliest passive vibration isolator is a

linear one with a single-degree-of-freedom system. The threshold limit for the execution of vibration attenuation in a linear system is a square root of two times of natural frequency of the system. These characteristics limit using a linear system to a high-frequency range only. In the past, the isolation system having low natural frequency was designed at the cost of large static deflection, which caused the system to wobble and finally break down. This weakness or problem can be overcome by introducing the active or semi-active system, which has the shortcomings of complexity and reliability [2]. To resolve this issue, nonlinearity can be introduced into the passive vibration isolator to possess high static stiffness to support large static deflection and low dynamic stiffness to widen the frequency range of isolation [3].

Nonlinearity can be introduced either by nonlinear stiffness [4] or by nonlinear damping [5]. The progress in nonlinear vibration isolators with different designs is reviewed in the literature [3, 6, 7]. Quasi-zero-stiffness is a representative design with nonlinear stiffness that exhibits large static stiffness to support large weight and low dynamic stiffness to attenuate the external vibration [8–11]. If the structure's parameters are properly designed, QZS isolators can exhibit ultra-low stiffness, zero stiffness, or negative stiffness [12, 13]. Many QZS isolators are available in the literature, but the archetypal one consists of three spring mechanisms. A vertical spring providing positive stiffness is connected in parallel with two oblique springs that provide negative stiffness. This prototype exhibits a small region of quasi-zero stiffness, which is ideal for isolating the vibration due to the low natural frequency in that region. Meanwhile, the large load capacity provided by the vertical spring element overcomes the disadvantage of the linear isolators.

The research work by Carrella et al. [10] has all the preliminary theoretical concepts on the QZS type of isolator, including static analysis, static optimization of geometrical parameters [14], dynamic analysis, including both force and motion transmissibility [15, 16]. The three-spring isolator considering stiffness nonlinearity is also studied in [17] and applied for shock isolation [18]. Liu et al. [19] established another model based on the three-spring mechanisms and did an accurate dynamic study. A scissor-like structure with an extra inertial element is proposed in [20–22] to achieve a better isolation performance. Euler buckled beam is used for passive vibration isolation and shock

absorption [20–23]. The sliding beam was used by Huang et al. [27] to exhibit a negative stiffness module for an ultra-low-frequency vibration isolator. Apart from these designs, the QZS/HSLDS characteristics were also obtained from torsional magnetic spring design [24, 25], bionic design [26], and six-degree platform design [27, 28]. It can be observed from the above-mentioned research results that the quasi-zero-stiffness region realizes a wider effective vibration isolation region and also reduces the force and motion transmissibility. Therefore, the QZS isolator has a broad application prospect as a passive vibration isolator.

Zhou et al. [29] attenuated vibration in a low-frequency range using an HSLDS resonator; the unit cell of the resonator achieved QZS property using two oblique and one vertical spring. The unit cell was placed periodically in a beam to form a metastructure. Wang et al. [30] designed an HSLDS resonator using four oblique springs and one vertical spring to exhibit the QZS property. Wen et al. [31] achieved QZS property using six oblique springs and one vertical spring. The unit cell was then used to achieve vibration isolation in the low-frequency range. Han et al. [32] designed a metastructure using an elliptical ring. Under compression, the elliptical ring exhibited QZS property, and further, the desired vibration isolation was achieved by adjusting the eccentricity of the elliptical ring.

However, the QZS isolator described in the previous research mainly focuses on the application of vibration isolation for vehicle seats, engines, etc., where the large-scale individual structure was used. For the microdevices, precision instruments, and other small devices, the installation of spring mechanism will be difficult to ensure vibration isolation performance. Therefore, there is a need for continuous structure with QZS material property similar to the precision instrument or microdevices that can be used as a vibration isolator. With the rapid development in additive manufacturing, metastructures can be used for vibration isolation with advanced mechanical and physical properties. As the material properties of the metastructure are strictly dependent upon the physical arrangement of the interior periodic unit cells, different unit cells with negative stiffness properties are proposed as curved beam in [33–36] and as inclined beam in [37, 38]. The negative stiffness is obtained from these unit cells by buckling or snap-through

behavior, which is the main principle behind the energy absorption of metastructures [39, 40]. This unit cell can be arranged accordingly to form a metastructure, which can be used for energy absorption or shock performance. Thus, it opens a new pathway to explore continuous structure fabricated using 3D printing for vibration isolation in the micro-machine industry.

This work is concerned with a QZS vibration isolator composed of cosine beam system and semicircular arches connected in parallel and to study its static characteristics and dynamic behavior. Firstly, the design of the metastructure is discussed in Sect. 2, along with the mechanical behavior of the unit cell possessing QZS property. Then, the static characteristics of the metastructure under uniaxial compression are discussed in Sect. 3. Following that, dynamic behavior and vibration isolation property of the metastructure are investigated in Sect. 4. Stability analysis is performed in Sect. 5. At last, the conclusion is discussed in Sect. 6.

2 Design of prototype

2.1 Structural model

The unit cell of the QZS model used in this work consists of three springs connected in parallel. The horizontal/oblique spring provides the negative stiffness, and two similar vertical springs support the isolated mass and exhibit positive stiffness. The overall system is vertically symmetrical. The model designed in this work is shown in Fig. 1; the unit cell consists of two semicircular arches, two cosine modulated curved beams, and stiffer walls. Under the lateral load, the clamped cosine curved beams will possess negative stiffness together due to the buckling or snap-through behavior.

The semicircular arch will possess positive stiffness due to bending-dominated behavior under the vertical load. As shown in Fig. 1c, the shape of the cosine beam is given by the equation

$$y = \frac{h}{2}\left(1 - \cos\left(2\pi \frac{x}{l_1}\right)\right) \tag{1}$$

where l_1 is the length, h is the amplitude, t_1 is the thickness, and b_1 is the depth of beam. The semicircular arc shown in Fig. 1d has length l_2, thickness t_2,
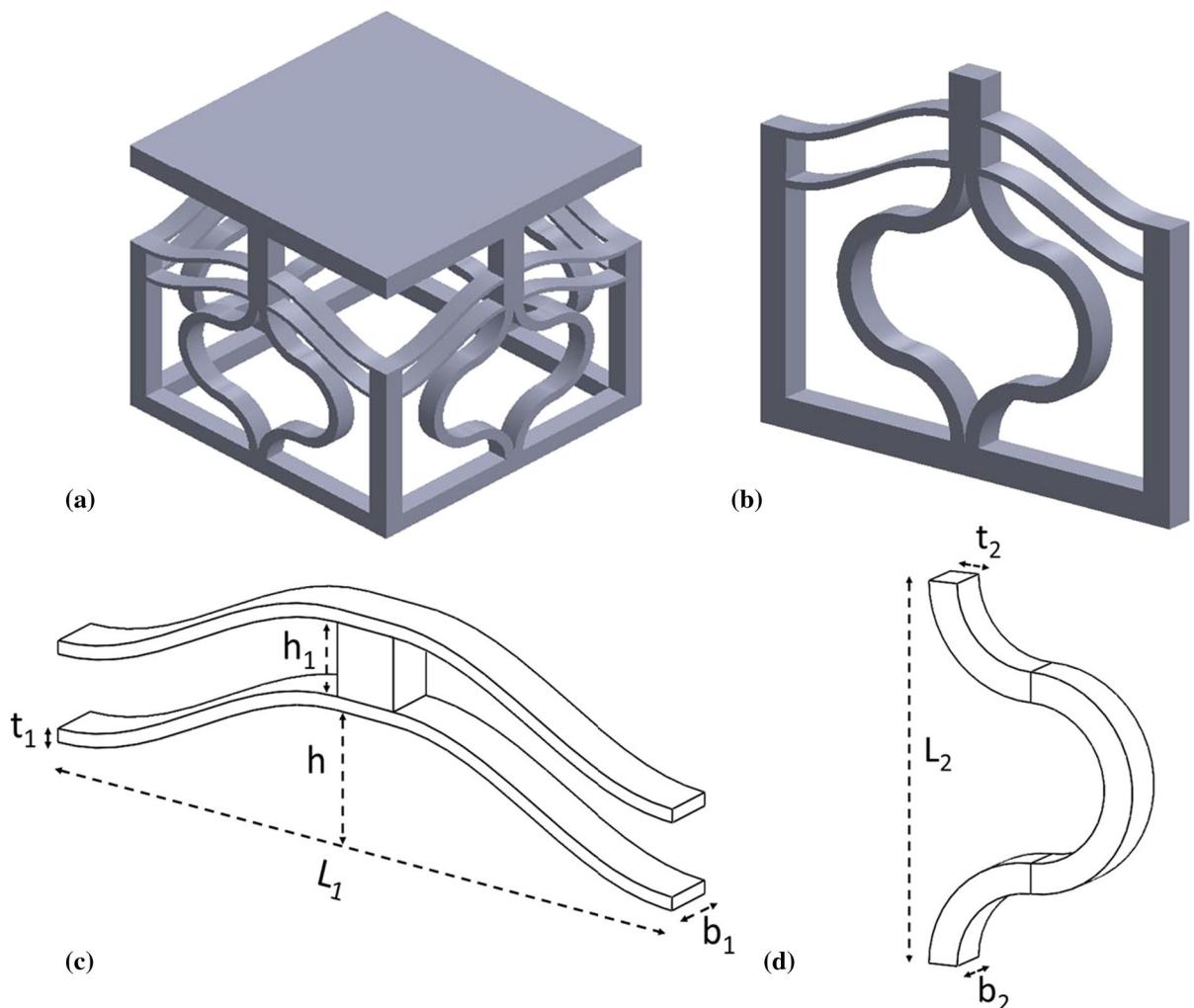
depth b_2, and radius $R = l_2/4$. The cosine beam and semicircular arches are then connected with the stiffness wall of thickness t. By arranging the positive stiffness arches and negative stiffness beam in parallel, the unit cell shown in Fig. 1b is expected to possess a quasi-zero-stiffness (QZS) region. The unit cell is then arranged in parallel to form a 3D metastructure shown in Fig. 1a. A QZS property can be realized by properly designing the unit cell for different applications.

2.2 Mechanism behind the metastructure
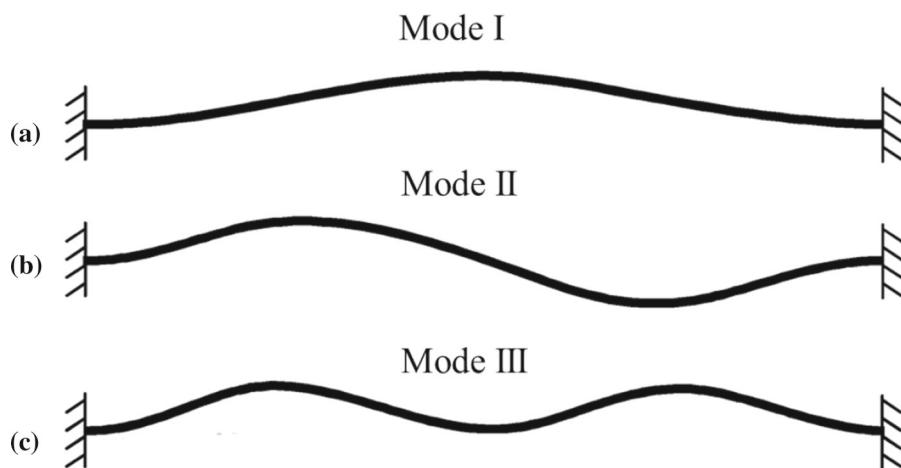
The mechanical behavior of the cosine beam subjected to lateral displacement at the center can be studied using the modal superposition of buckling modes of a straight beam clamped at both ends [41]. When a straight beam clamped at both ends is deformed laterally by force acting at its center, it shows certain mode shapes as shown in Fig. 2, out of which the first two-mode shapes are of the main focus in this work. By properly designing the beam, the snap-through behavior leading to a bistability mechanism can be achieved. A common bistable mechanism involves a prestressed straight beam to buckled into its first mode, and this mode shape can be used as the initial design of a stress-free cosine curved beam, as shown in Fig. 2a.

According to Qiu et al. [42], the structural energy inside the curved beam during deflection consists of compression energy and bending energy. From an energy point of view, the bending energy increases monotonically during the downward deflection of the curved beam. In contrast, the compression energy increases to maximum up to the centerline and then decreases after crossing the centerline. If the curved beam is designed so that the decrease in compression energy after crossing the centerline is faster than the increase in the bending energy due to the snap-through, this results in a negative force region (as shown in Fig. 3a) exhibiting a negative stiffness region. This is also an indication of bistability. For designing such a curved beam, it should hold two conditions: (a) height-to-thickness ratio of the beam should be greater than or equal to 6, (b) the second mode (Fig. 2b) of straight clamped–clamped beam should be constrained [43].
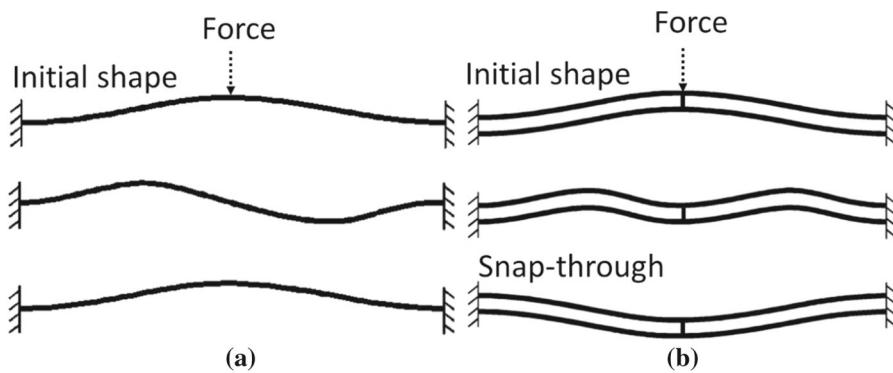
The first condition can be satisfied easily by the proper designing of the beam. The most effective method to satisfy the second condition is to clamp two cosine curved beams together at the center, referred to

Fig. 1 **a** Metastructure or 3D model, **b** unit cell, **c** cosine beam system, **d** semicircular arch

Fig. 2 Mode shapes of a straight beam clamped at both ends. **a** First mode, **b** second mode, **c** third mode

Fig. 3 Mechanism of the **a** single curved beam, **b** bistable double-curved beam under vertical load [42]

as double curved beam structure [43]. The center clamp helps in shifting the rotational motion of either beam center to the axial motion of the other beam. As both the beams are stiff in the axial direction, the beam's rotational motion can be scaled down. If the length of the center clamp is considered to be more than five times the thickness of the cosine curved beam, then the second mode can be completely constrained [42]. The difference between the mechanism of a single curved beam and double curved beam is shown in Fig. 3, where the respective beams are compressed with a vertical force.

A double cosine curved beam structure (shown in Fig. 4b) is designed based on the above-mentioned condition for discussing the effect of snap-through behavior. From the force–displacement curve of the cosine beam (shown in Fig. 4a) under the displacement control, it can be observed that, as the displacement increases, the force increases up to a certain value. Beyond this point, as the displacement increases, force decreases because the second mode shape is restricted. A further increase in the displacement leads the curved beam to reach the other stable state, and therefore the force increases again and reaches the initial value. Thus, the double cosine beam under the vertical force snaps through from one stable (Fig. 4b) to another stable state (Fig. 4d) through the negative stiffness mechanism. The negative stiffness can be observed in the force–displacement region of Fig. 4a.

The unit cell (shown in Fig. 5b) designed in this work is inspired by the spring–mass system depicted in Fig. 5a. The spring–mass system consists of two horizontal springs having stiffness k_h connected in

parallel with the two vertical springs having stiffness k_v. The unit cell designed in this work consists of one double cosine beam system connected in parallel with two semicircular arches, as shown in Fig. 5b.

The cosine beam provides negative stiffness, and semicircular arches exhibit positive stiffness. When the parameters of the cosine beam satisfy the bistability conditions, the force–displacement curve of the cosine beam can be approximately represented by three straight lines (shown in Fig. 5c). Qiu et al. [42] derived the designing parameter *(Q)* of the cosine beam system and the force and displacement parameters mentioned in Fig. 5c. The designing parameter Q and the corresponding force–displacement parameters are represented by the following equations:
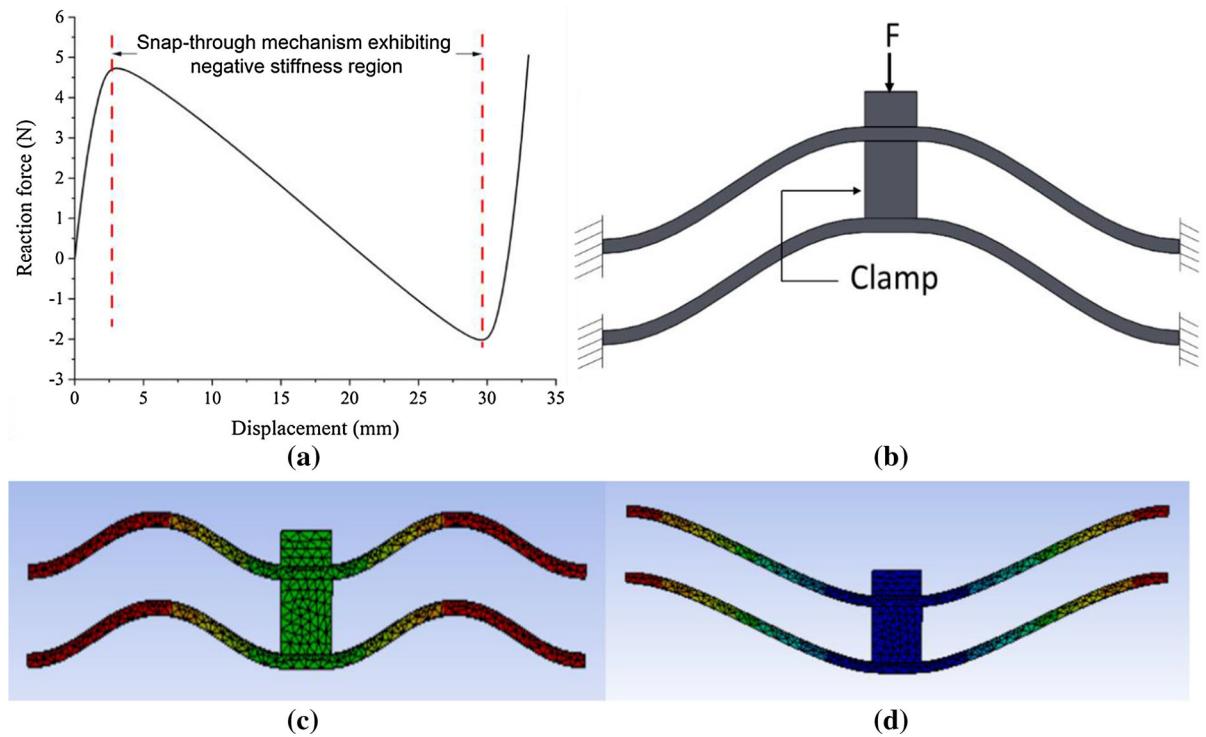
$$Q = \frac{h_1}{t_1} = 6 \tag{2}$$

$$f_{top} \approx 16\pi^4 \frac{E_1 I_1 h_1}{l_1^3} \approx 1480 \frac{E_1 I_1 h_1}{l_1^3} \tag{3}$$

$$f_{bottom} \approx -8\pi^4 \frac{E_2 I_2 h_1}{l_2^3} \approx -740 \frac{E_2 I_2 h_1}{l_2^3} \tag{4}$$

$$d_{top} = 0.16h, \quad d_{bottom} = 1.92h, \quad d_{end} = 1.99h \tag{5}$$

Here, I_1 is the moment of inertia of cosine beam, L_1 is the length of cosine beam, h is the height of cosine beam, I_2 is the moment of inertia of semicircular arch, and L_2 is the length of semicircular arch. E_1 and E_2 are the modulus of elasticity of cosine beam and semicircular arch, respectively. It can be observed from the force–displacement curve (shown in Fig. 5c) that, for the double cosine beam system, there are three linear stiffness regions. The first stiffness region is k_{c1}; the

Fig. 4 **a** Schematic force–displacement curve of cosine beam exhibiting negative stiffness region, **b** initial shape of double cosine beam system, **c** transition state of cosine beam after application of force, **d** snap-through mechanism leading to the bistable state of cosine beam

second is negative stiffness region k_{c2} that counteracts with the positive stiffness (k_s) provided by semicircular arches to yield the QZS property; further, the third stiffness region is k_{c3}. The stiffness of the beam for the three stages (0–I)-k_{c1}, (I–II)-k_{c2}, and (II–III)-k_{c3} can be derived from the force–displacement curve as

$$k_{c1} = 9250 \frac{E_1 I_1}{l_1^3}, \quad k_{c2} = -1253.18 \frac{E_1 I_1}{l_1^3},$$
$$k_{c3} = 10571.42 \frac{E_1 I_1}{l_1^3} \tag{6}$$

The semicircular beam is primarily bending-dominated, and under the vertical displacement, the semicircular arch shows constant positive stiffness. The force–displacement curve varies linearly (Fig. 5c). The stiffness of the semicircular arch can be derived as [44]

$$k_s = 18.257 \frac{E_2 I_2}{l_2^3} \tag{7}$$

As the cosine beam system and semicircular arches are connected in parallel, the equivalent stiffness of the unit cell under vertical displacement is the sum of individual stiffness. Hence, the force–displacement behavior of the unit cell can be obtained as three connected approximate straight lines shown in Fig. 5d. The stiffness expression of the unit cell for all the three regions can be obtained as follows:
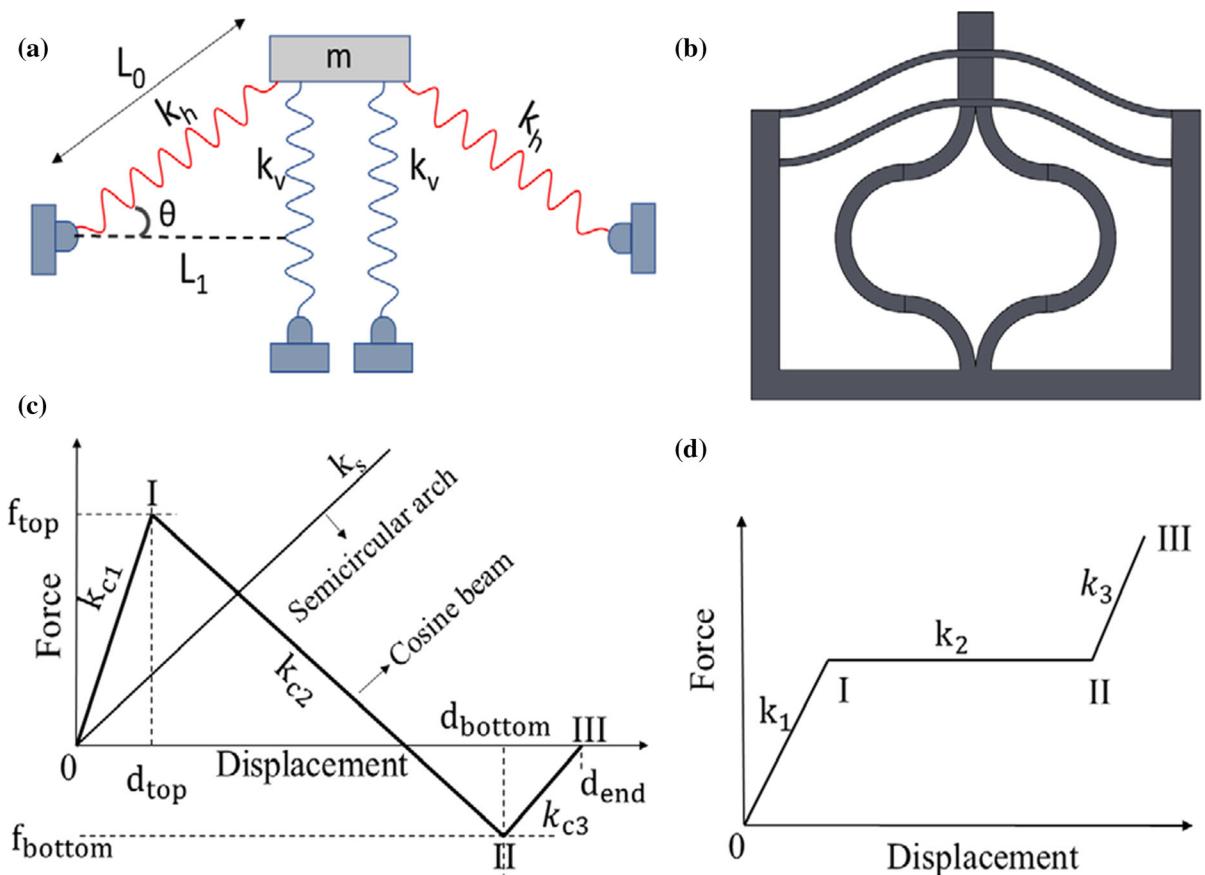
$$k_1 = k_{c1} + 2k_s \quad k_2 = k_{c2} + 2k_s \quad k_3 = k_{c3} + 2k_s \tag{8}$$

From the curve shown in Fig. 5d, the region between I and II can be observed as the QZS region. Hence, equating the stiffness k_2 to zero will give the relation between the cosine beam system (horizontal spring) and semicircular arches (vertical spring) for achieving the QZS property.

$$k_2 = k_{c2} + 2k_s = 0 \tag{9}$$
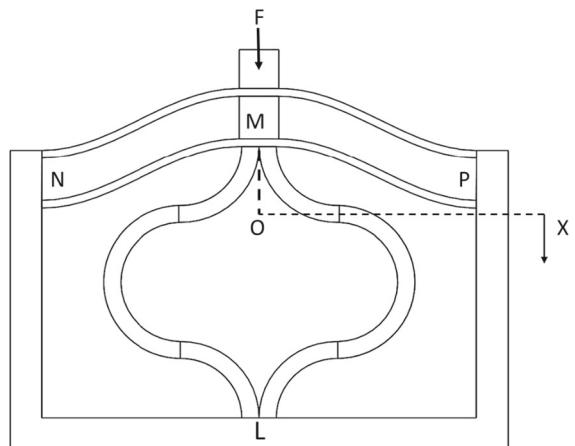
As the objective of this work is to design the system for QZS condition, Eq. (9) needs to be satisfied. The spring–mass system shown in Fig. 5a is then used as a reference to derive the relation between the stiffness ratio μ and geometrical parameter γ derived in the

(a)

(b)

(c)

(d)

Fig. 5 **a** Spring–mass system, **b** unit cell showing the arrangement of cosine beam system and semicircular arches, **c** the approximate force–displacement curve of cosine beam and semicircular arch, **d** approximate force–displacement curve of unit cell

upcoming section in Eq. (27). Further, the obtained value of the geometrical parameter is used to design the cosine beam system with appropriate dimensions.

Considering the unit cell model shown in Fig. 6, double cosine beam system is clamped to the stiff wall at points N and P, and the semicircular arch is clamped to the stiff wall at point L. Here, both the beams of the double cosine beam system have the same configuration. The cosine beam is connected to the semicircular arch at point M. The application of vertical force (F) causes the cosine beam to deflect from its initial position M to a static equilibrium position O. After the point O, the cosine beam starts possessing negative stiffness k_{c2}; this is the stiffness shown between the region I and II (shown in Fig. 5). Position O is considered as the static equilibrium point for all the analyses performed throughout this work. The unit cell starts exhibiting QZS behavior after the further downward deflection from point O.

Fig. 6 Schematic of unit cell model. Force (F) acting at the top of cosine beam, X is the static equilibrium position of the combined unit cell

Let's consider the unit cell as a spring–mass system shown in Fig. 5a, where the double cosine beam system acts as a horizontal spring whose stiffness k_h is related to k_{c2} as

$$k_h \sin \theta = k_{c2} \qquad (10)$$

Here, the vertical component of equivalent stiffness of horizontal spring is considered as k_{c2}. The semicircular arches act as vertical springs whose stiffness is considered as k_s. When the unit cell experiences a vertical displacement X from the static equilibrium position, the force exerted by the cosine beam is

$$F_h = k_h \left(L_0 - \sqrt{L_1^2 + X^2} \right) \qquad (11)$$

Here, L_0 is the original length of beam without any deformation (i.e., at point M). L_1 is the projected length of cosine beam on the horizontal plane. The vertical component of the cosine beam is the restoring force for the negative stiffness mechanism (NSM):

$$F_{NSM} = -F_h \sin \theta \qquad (12)$$

Here, θ is the angle between the cosine beam and horizontal plane, and $\sin \theta$ is given by

$$\sin \theta = \frac{X}{\sqrt{L_1^2 + X^2}} \qquad (13)$$

Substituting Eq. (13) into Eq. (12), the restoring force–displacement relation of NSM is given by

$$F_{NSM}(X) = -k_h \left(\frac{L_0}{\sqrt{L_1^2 + X^2}} - 1 \right) X \qquad (14)$$

The force–displacement relationship of semicircular arch is given by

$$F_v = 2k_v X \qquad (15)$$

Here, k_v is the stiffness of semicircular arch. The QZS unit cell is a parallel combination of cosine beam and the semicircular arch; the force–displacement relationship of unit cell is given by

$$F_{QZS}(X) = F_v + F_{NSM}(X) \qquad (16)$$

$$F_{QZS}(X) = 2k_v X - k_h \left(\frac{L_0}{\sqrt{L_1^2 + X^2}} - 1 \right) X \qquad (17)$$

Equation (17) can be written in non-dimensional form by introducing new terms:

$$f_{QZS}(x) = \frac{F_{QZS}}{k_v L_0}, \quad \mu = \frac{k_h}{k_v}, \quad \gamma = \frac{L_1}{L_0}, \quad x = \frac{X}{L_0} \qquad (18)$$

Here, μ is the stiffness ratio and γ is the geometrical parameter.
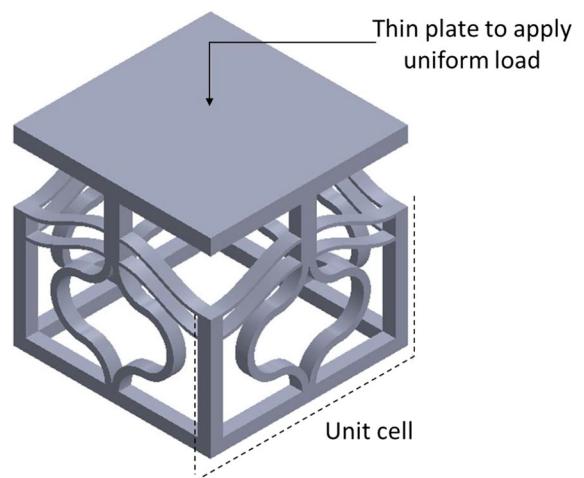
$$f_{QZS}(x) = 2x - \mu \left(\frac{1}{\sqrt{\gamma^2 + x^2}} - 1 \right) x \qquad (19)$$

Equation (19) represents the non-dimensional force–displacement relation for a unit cell. The force–displacement characteristics of the metastructure are discussed in the next section.

3 Static analysis

3.1 Analytical modeling

The design discussed in Sect. 2.2 consists of a cosine beam connected in parallel with the semicircular arches, and both are connected to stiffer walls. Once this unit cell is deformed beyond the static equilibrium point, QZS behavior can be achieved. A metastructure is designed based on the parallel arrangement of a four-unit cell with one thin plate kept on the top to apply a uniform load over all the unit cells, as shown in Fig. 7. According to the parallel spring theory, when the springs are arranged in parallel, the equivalent stiffness is the sum of the individual stiffness of each

Fig. 7 Metastructure or 3D model obtained by arranging the unit cell

spring acting under a uniform force. As the stiffness of unit cell is given by

$$k_{\text{unitcell}} = k_{c2} + 2k_s = k_h \sin \theta + 2k_v, \qquad (20)$$

the equivalent stiffness of the metastructure is given as

$$K_{\text{eq}} = 4 * k_{\text{unitcell}} = 4k_{c2} + 8k_s \qquad (21)$$

Based on the parallel spring theorem, the force–displacement characteristics of the metastructure can be given as

$$F_{\text{QZS}}(X) = 4F_v + 4F_{\text{NSM}}(X) \qquad (22)$$

Substituting Eqs. (14) and (15) in Eq. (22),

$$F_{\text{QZS}}(X) = 8k_v X - 4k_h \left(\frac{L_0}{\sqrt{L_1^2 + X^2}} - 1 \right) X \qquad (23)$$

Equation (23) can be written in non-dimensional form by substituting Eq. (18):

$$f_{\text{QZS}}(x) = 8x - 4\mu \left(\frac{1}{\sqrt{\gamma^2 + x^2}} - 1 \right) x \qquad (24)$$

The non-dimensional stiffness–displacement characteristics can be calculated by differentiating Eq. (24) with respect to non-dimensional coefficient x:

$$k_{\text{QZS}}(x) = 8 + 4\mu - \frac{4\mu\gamma^2}{(\gamma^2 + x^2)^{3/2}} \qquad (25)$$

It can be observed that the stiffness is minimum at the static equilibrium position ($x = 0$). To achieve a desired stable QZS characteristics, k_{QZS} at static equilibrium is set equal to zero and a unique relation between the geometrical parameter γ and stiffness ratio μ is derived (elaborated in "Appendix A").

$$k_{\text{QZS}}(0) = 8 + 4\mu \left(1 - \frac{1}{\gamma} \right) = 0 \qquad (26)$$

$$\mu_{\text{QZS}} = \frac{2\gamma}{1 - \gamma}, \quad \gamma_{\text{QZS}} = \frac{\mu}{\mu + 2} \qquad (27)$$

It is clear that the stiffness at the static equilibrium position is negative and unstable if $\gamma < \gamma_{\text{QZS}}$ or $\mu > \mu_{\text{QZS}}$ (elaborated in "Appendix B"). It is obvious to avoid the negative stiffness due to the instability issues. For isolation purposes, it is better to achieve positive stiffness at the equilibrium position by choosing the parameters based on the condition $\gamma > \gamma_{\text{QZS}}$ or $\mu < \mu_{\text{QZS}}$. In the subsequent analysis,

Eq. (27) is always held to ensure the stable quasi-zero-stiffness behavior.

The non-dimensional force as a function of non-dimensional displacement (Eq. 24) is plotted in Fig. 8 for different values of γ, when $\mu = \mu_{\text{QZS}}$. QZS region is observed when the value of f_{OZS} remains zero for varying x. The range of QZS increases with γ.

The non-dimensional stiffness–displacement characteristic is plotted in Fig. 9 for varying values of γ, when $\mu = \mu_{\text{QZS}}$. At the static equilibrium position, the negative stiffness obtained by the cosine beams is perfectly balanced by the positive stiffness incorporated by the semicircular arches, thus making the combined stiffness zero. The same can be observed in Fig. 9 at $x = 0$.

From the stiffness–displacement curve shown in Fig. 9, it can be observed that for a certain range of displacement depending upon μ, the stiffness value of the QZS isolator is less than that of the equivalent linear isolator. The displacement range which satisfies the lower stiffness value of the QZS isolator is referred to as low-stiffness–displacement range; it is an important indicator of the stiffness–displacement characteristics and can be calculated by keeping the stiffness value of the QZS isolator less than that of the equivalent linear isolator (elaborated in "Appendix C"):

$$k_{\text{QZS}}(x) < 8 \qquad (28)$$

$$|x| < \gamma^{2/3} \sqrt{1 - \gamma^{2/3}} \qquad (29)$$
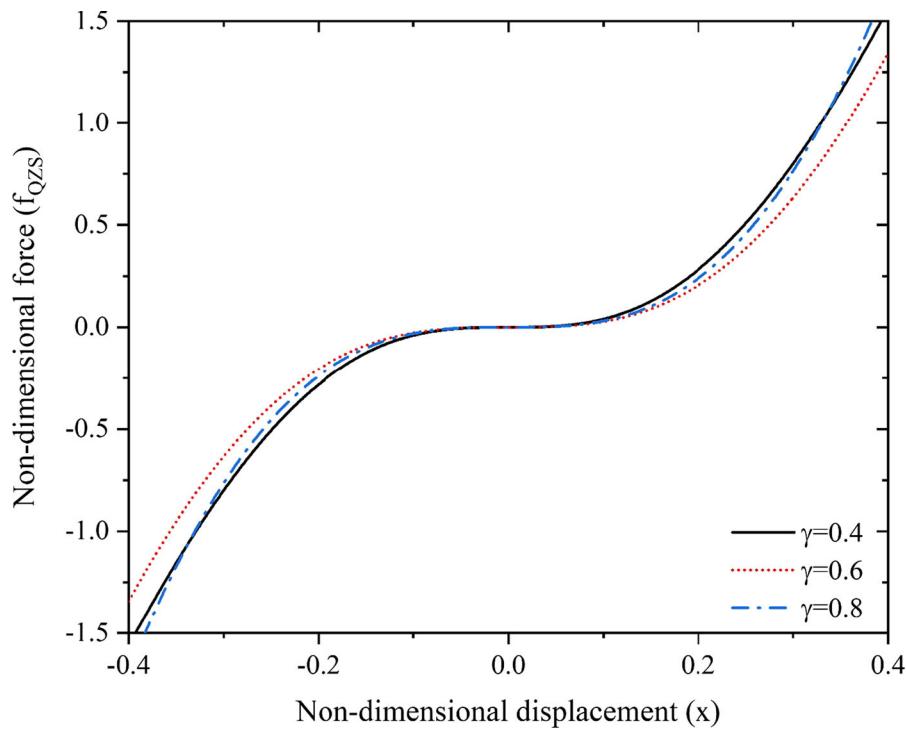
$$L_{\text{sd}} = 2x = 2\gamma^{2/3} \sqrt{1 - \gamma^{2/3}} \qquad (30)$$

Here, L_{sd} is the length of low-stiffness–displacement range. The maximum value of L_{sd} can be obtained by differentiating Eq. (30) with respect to γ and equating it to zero. The solution suggests that L_{sd} is maximum at $\gamma = 0.5443$. Figure 10 shows the variation of low-stiffness–displacement range with respect to geometrical parameter γ.

$$\max L_{\text{sd}}(\gamma = 0.5443) = 0.7698 \qquad (31)$$
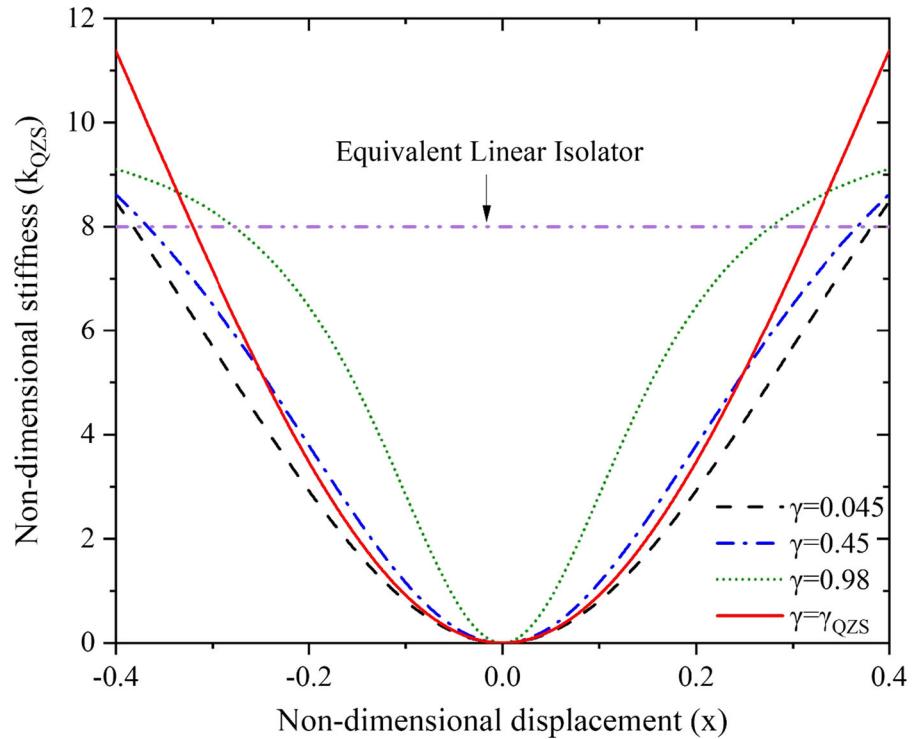
3.2 Design of the model

In this work, the metastructure is designed to exhibit a quasi-zero stiffness region, as well as a positive
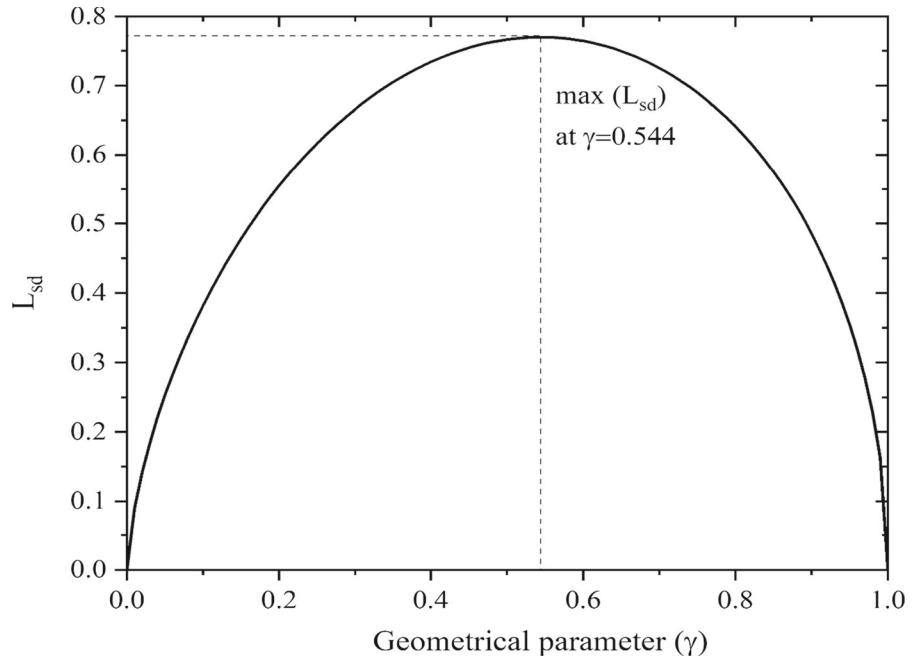
Fig. 8 Force–displacement curve of metastructure for varying γ, when μ and γ satisfy Eq. (27)

Fig. 9 The stiffness–displacement curve of metastructure for varying γ, when μ and γ satisfy Eq. (27)

Fig. 10 Length of low-stiffness–displacement region as a function of geometrical parameter γ

stiffness region to withstand the weight of an isolated object. The parameters of the unit cell designed in this work are shown in Table 1.

The stiffness values k_{c1}, k_{c2}, k_{c3}, and k_s can be calculated using Eqs. (6) and (7).

The region I–II shown in Fig. 5 demonstrates the negative stiffness region (k_{c2}) for the cosine curved beam and positive stiffness region (k_s) for the semi-circular arches. For achieving the quasi-stiffness region, the negative stiffness should become equal to the positive stiffness. From Eq. (21), it can be seen that

$$K_{eq} = 0 = 4k_{c2} + 8k_s \tag{32}$$

Let's consider

$$\mu = 2, \quad \gamma = 0.5 \tag{33}$$

The value of γ is obtained from Eq. (27). From the force–displacement characteristics of a QZS structure studied in Eq. (24) and shown graphically in Fig. 8, it can be observed that the curves have a shape similar to that of a cubic polynomial. Taylor series expansion is

one of the ways to approximate a polynomial function. The force can be expressed as a power of series order N.

$$f(x) = f(x_o) + \sum_{n=1}^{N} \frac{f^n(x_o)}{n!}(x - x_o)^n \tag{34}$$

The system is expanded at x_0, and f^n denotes the n_{th} derivative of function f. Since the interest in this analysis is about the static equilibrium position, the power series is expanded about the equilibrium point. By expanding Eq. (24) using Eq. (34) and substituting $x_0 = 0$, the expression for the force can be approximated as (elaborated in "Appendix D")

$$f(x) = \left[4\mu\left(\frac{\gamma - 1}{\gamma}\right) + 8\right]x + \frac{2\mu}{\gamma^3}x^3 - \frac{3\mu}{2\gamma^5}x^5 + \frac{5\mu}{4\gamma^7}x^7 \tag{35}$$

The force–displacement relationship for the QZS case is derived in terms of geometrical parameter γ by substituting Eq. (27) into Eq. (35):

Table 1 Parameters of unit cell

Parameters	L_1	t_1	b_1	h	L_2	t_2	b_2
Values	50 mm	1 mm	4 mm	8 mm	35 mm	2.28 mm	4 mm

$$f_{QZS}(x) = \frac{4}{(1-\gamma)\gamma^2}x^3 - \frac{3}{(1-\gamma)\gamma^4}x^5 + \frac{5}{2(1-\gamma)\gamma^6}x^7 \tag{36}$$

The approximated non-dimensional force–displacement characteristics described in Eq. (36) for different orders are plotted in Fig. 11 along with the exact expression obtained in Eq. (24). It can be observed that the fifth-order gives a good approximation with the exact expression. This can also be seen in Fig. 12, where the error percentage between the approximate and exact stiffness is plotted against the displacement. It can be seen that the error remains less (< 10%) for small displacements from the equilibrium position.

The fifth-order approximation of force–displacement characteristic can be written as

$$f_{app(QZS)}(x) = \alpha x^3 + \delta x^5 \tag{37}$$

Where, $\quad \alpha = \dfrac{4}{(1-\gamma)\gamma^2}, \quad \delta = -\dfrac{3}{(1-\gamma)\gamma^4} \tag{38}$

The non-dimensional stiffness–displacement relation can be approximated as

$$k_{app(QZS)}(x) = 3\alpha x^2 + 5\delta x^4 \tag{39}$$

Error percentage between the approximate stiffness and exact stiffness is given by
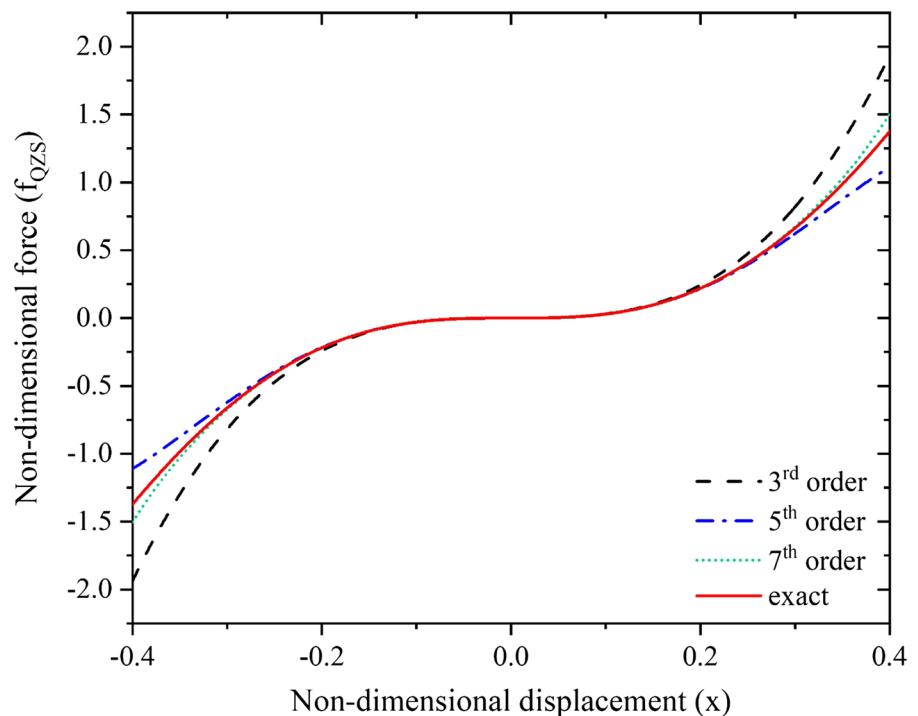
$$\text{Error}(\%) = \left| 1 - \frac{k_{app}}{k_{exact}} \right| * 100 \tag{40}$$

where k_{app} is given by Eq. (39) and k_{exact} is given by Eq. (25).
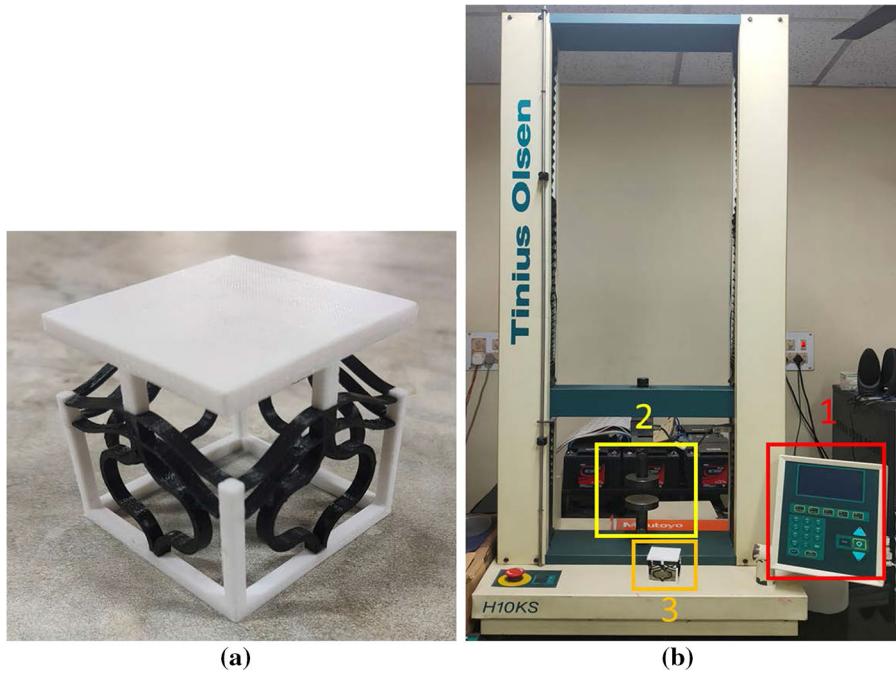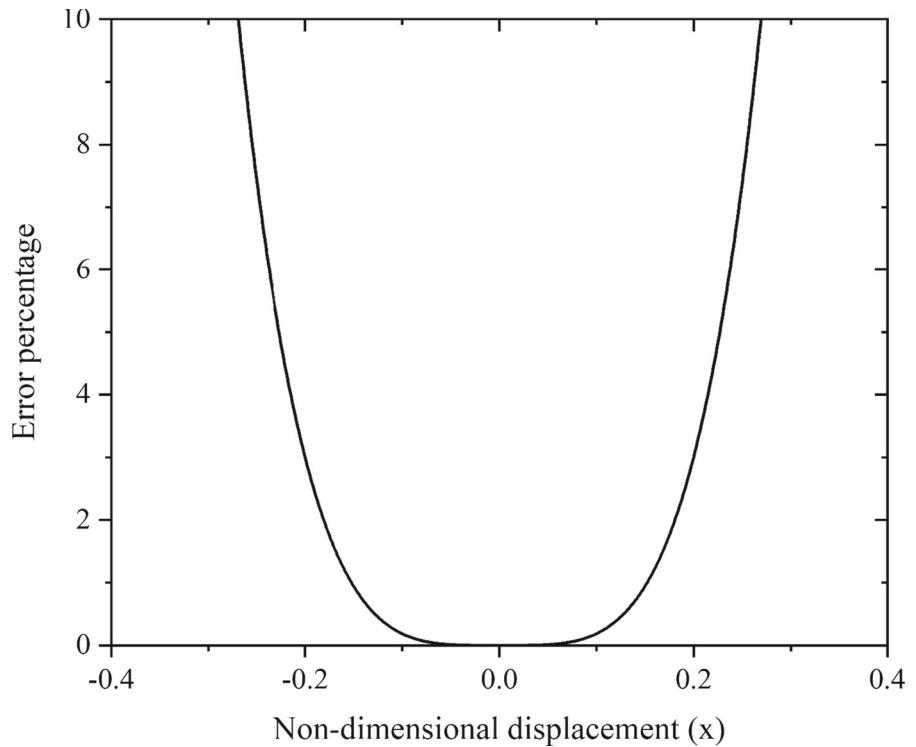
Therefore, the system can be designed based on the values $\gamma = 0.5, \mu = 2$. The system will isolate the vibration for relatively small displacements, as the fifth order of the Taylor series is considered for the approximate equation of force and stiffness in this work.

3.3 Quasi-static experiment

A uniaxial compression test is performed on the metastructure to study the mechanical behavior. The compression experiment is performed under displacement control with a strain rate of 1 mm/min. The reaction force–displacement curve obtained from the experiment will be used further to verify the numerical simulations. The metastructure used in this experiment is fabricated using PLA and TPU material. The high strength of PLA material provides fixed support to the

Fig. 11 Comparison of approximate and exact expression of non-dimensional force–displacement characteristics for the QZS system $\gamma = 0.5$, when $\mu = \mu_{QZS}$. The approximate expression of third, fifth, and seventh order

Fig. 12 The error between the approximate and exact stiffness relation, when $\gamma = 0.5$ and $\mu = \mu_{QZS}$

Fig. 13 a Metastructure sample—the white part is printed using PLA material, and black part is printed using TPU material, b experimental setup (1—instrument control system, 2—loading Jaw, 3—sample)

ends of the cosine beam system. The metastructure sample, along with the experimental setup, is shown in Fig. 13.

The constituent material used in this work is thermoplastic polyurethane (TPU), as it can be designed easily for different metastructure shapes because of its high toughness. A tensile test experiment is performed on the dog-bone sample fabricated based on the ASTM D638-14 using TPU material. The stress–strain curve is shown in Fig. 14. It can be observed that the TPU material exhibits hyperplastic properties.

3.4 Numerical simulation

In the present work, finite element analysis (FEA)-based simulation is performed to investigate the mechanical properties of the metastructure using ANSYS 19R3. To start with, the geometry is modeled in SOLIDWORKS 2020 software. Further analysis is performed in ANSYS static structural module with meshing using quadrilateral and triangular elements for compression tests (167,826 nodes and 77,558 elements), and mesh convergence was also performed to ensure accuracy. The above-mentioned element type supports the re-meshing criterion essential for the nonlinear deformation behavior owing to the buckling behavior of the metastructure.
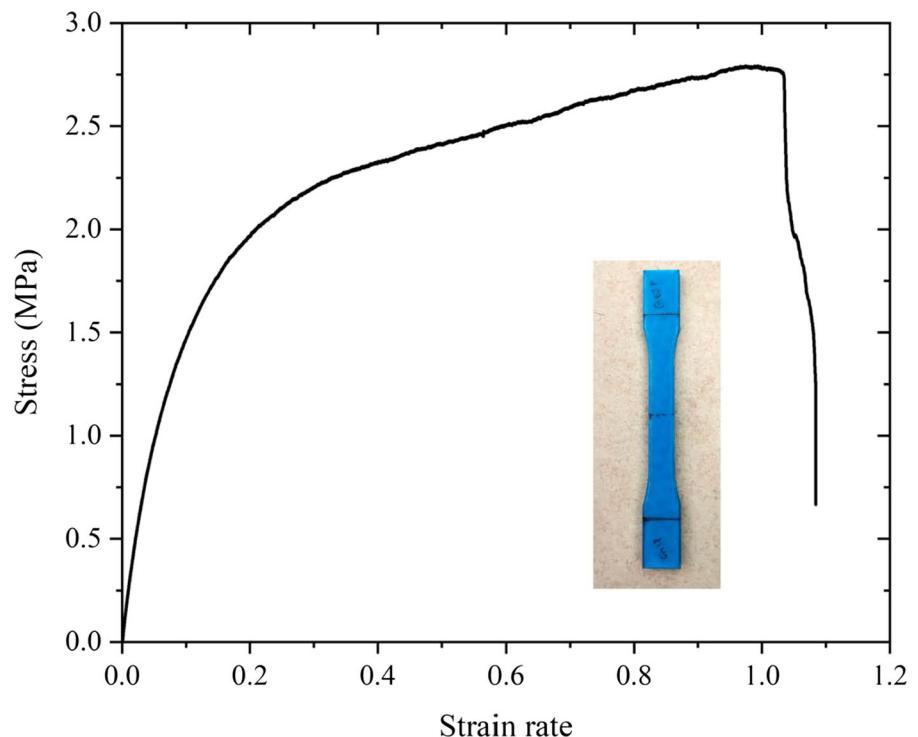
The boundary conditions are applied to imitate the real-time experiment. The bottom surface of the model is constrained in all six degrees of freedom (three rotations and three translations). The top surface is constrained in five degrees of freedom except for the vertical compression direction where the prescribed vertical displacement is applied. Theoretically, it is assumed that the stiffening walls of the model are rigid, and therefore all the left and right edges of the model are constrained. These boundary conditions are shown for the unit cell in Fig. 15.

3.5 Results and discussion
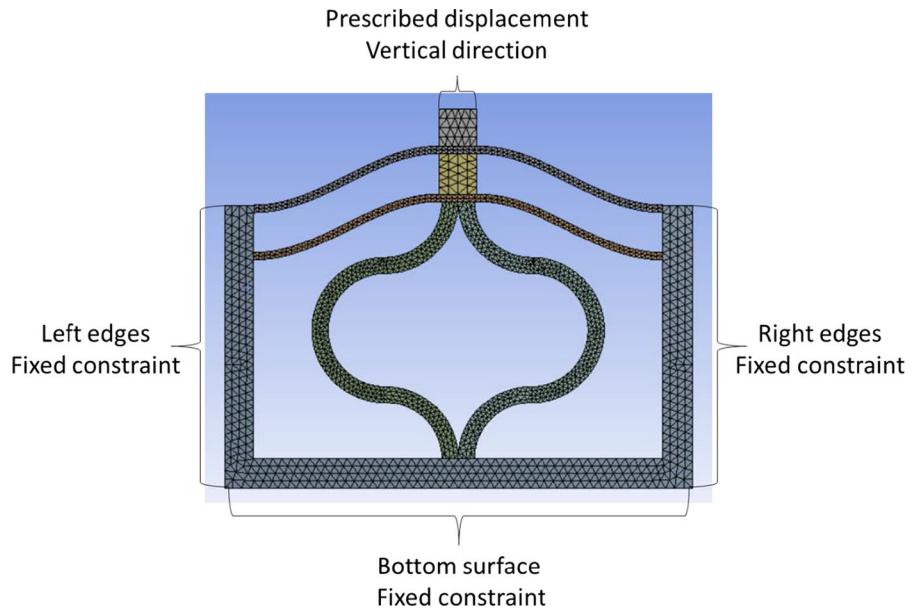
This section discusses the result of static analysis performed on the metastructure. The force–displacement characteristics of metastructure are shown in Fig. 16, followed by the deformation modes of the metastructure shown in Fig. 17.

The behavior of the metastructure under quasi-static vertical displacement can be observed based on three regions, as shown in Fig. 16. In the first region,
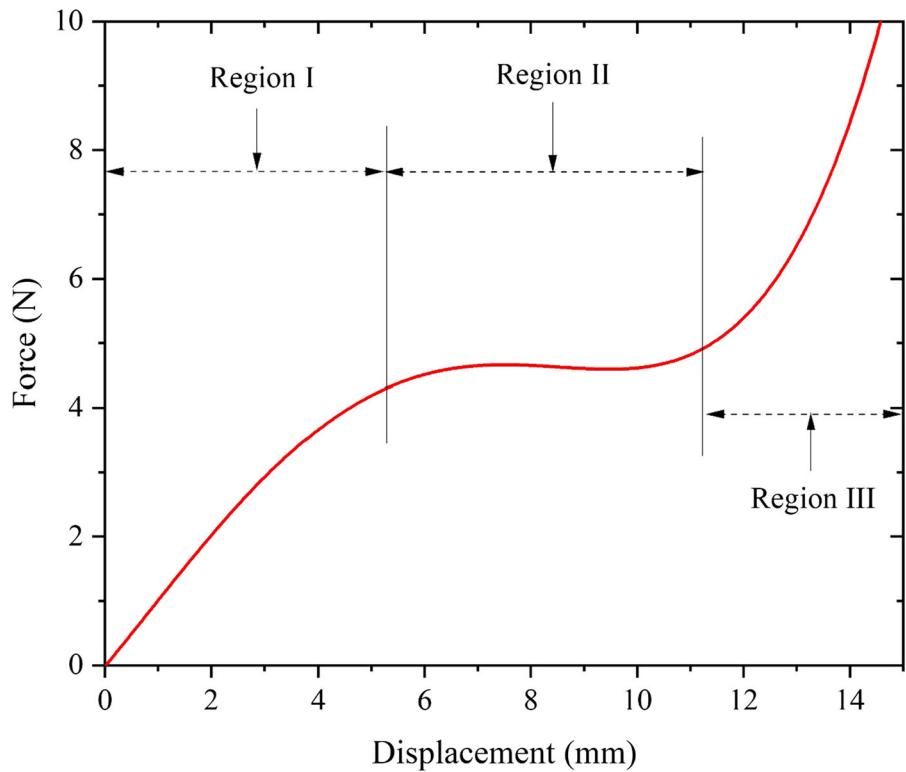

Fig. 14 Tensile test result of the manufactured dog-bone sample

**Fig. 15** Finite element model of a unit cell
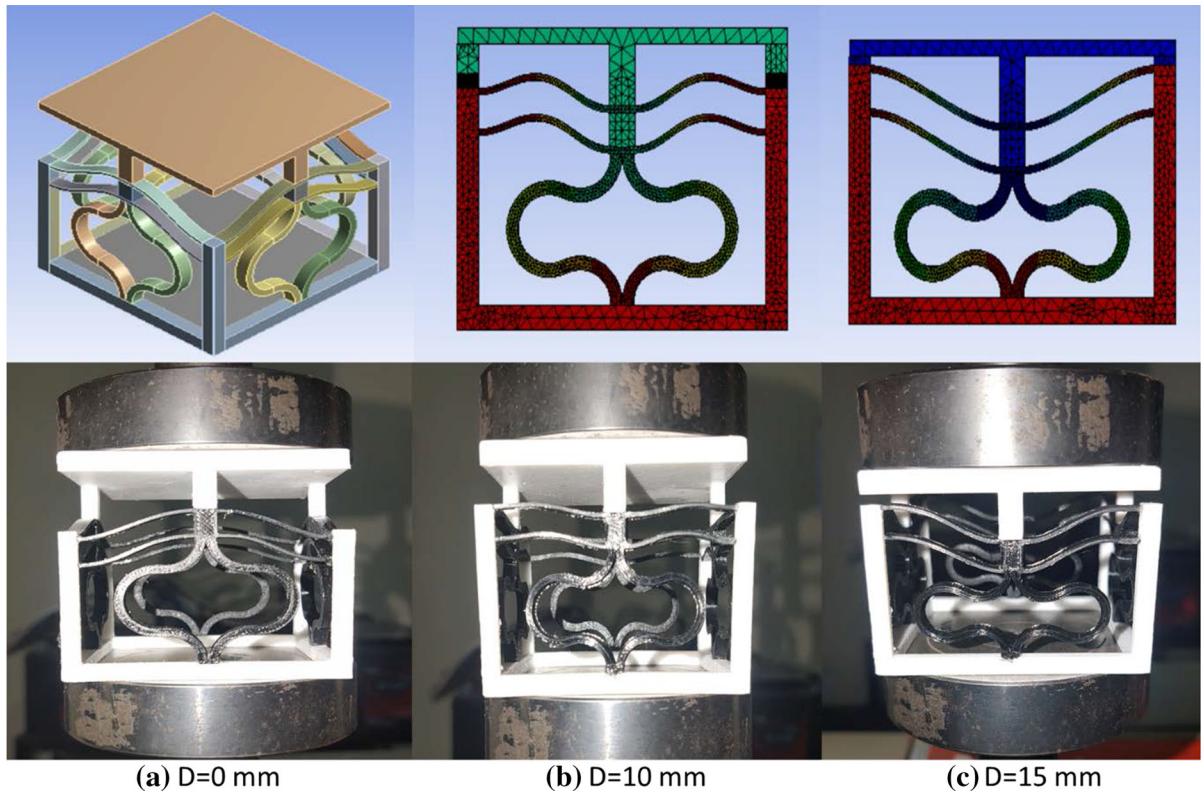
Fig. 16 Force–displacement curve obtained from experimental results for the metastructure representing three different regions

there is a sudden increase in the reaction force with the increase in compression displacement. This happens because at the initial stage, the cosine beam system and semicircular arches both act as linear spring and

exhibit positive stiffness in the loading direction. As the vertical displacement increases beyond the initial stage, the sudden shift of the metastructure stiffness from positive to quasi-zero level can be observed in

Fig. 17 Behavior of metastructure under different vertical displacements
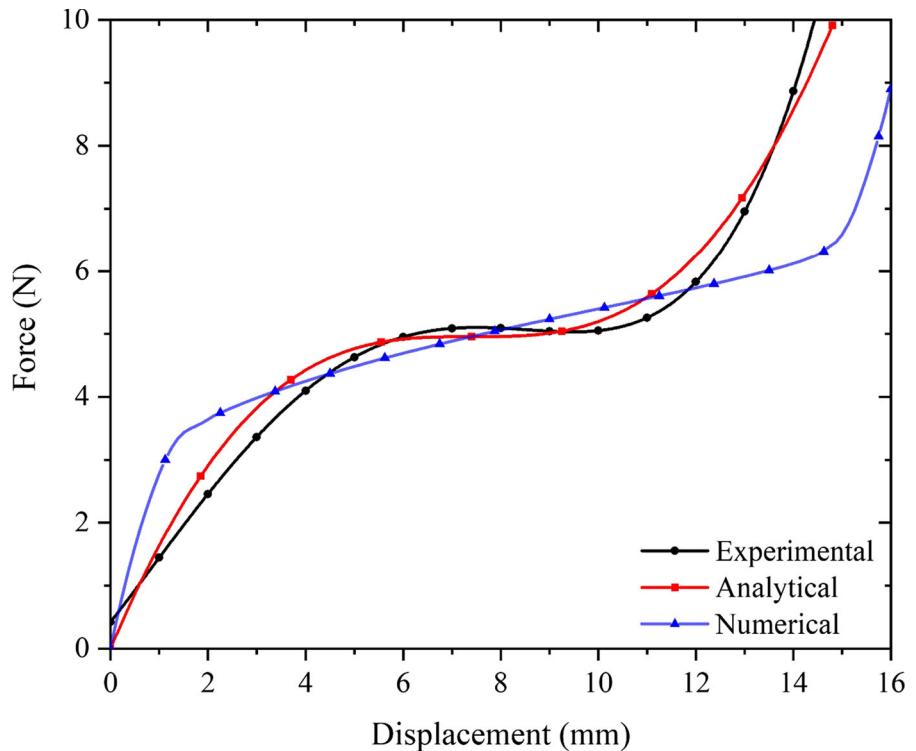
region II. This occurs because as the vertical displacement exceeds a certain value, the cosine beam system experiences a snapping-through behavior, resulting in the negative stiffness property of the cosine system beam. If the negative stiffness of the cosine system beam is equal to the positive stiffness of the semicircular arch, the equivalent stiffness of metastructure becomes zero, referred to as quasi-zero stiffness. With the further increase in vertical displacement, the metastructure experiences another shift in the stiffness from quasi-zero to positive value which can be seen in region III. This happens because of the sudden snapping-through of the cosine beam system to other stable state leading to the positive stiffness, which then combines with the positive stiffness of the semicircular arch to exhibit equivalent positive stiffness.

The response of the metastructure sample under different vertical displacements is captured and shown in Fig. 17, where the different deformation modes obtained from the experimental and numerical simulation are reflected. Figure 17a reflects the isometric view of the initial state of the metastructure. As the

displacement increases, the cosine beam system undergoes a snap-through behavior, and semicircular arches experience a bending-dominated deformation. It can also be observed from Fig. 17b that the cosine beam system experiences a symmetrical buckling behavior in the compression process; this leads to the native stiffness properties of the metastructure as obtained in Fig. 16. The other stable state of the cosine beam system can be observed in Fig. 17c. This stable state leads to the sudden shift of metastructure stiffness from quasi-zero to positive.

The results of the analytical and numerical solution are compared with the experimental results in Fig. 18. Firstly, the curve obtained from the analytical solution (Fig. 11) is converted into a dimensional form so that it can be compared with the experimental result. From Fig. 18, it can be found out that the analytical solution comes in good agreement with the experimental result; similarly, numerical simulation also reflected similar behavior except for the area of two transition phases between the quasi-zero and positive stiffness. This happens because the large deflection and nonlinear

Fig. 18 Comparison of the force–displacement curve of metastructure obtained from the experimental results, analytical solution, and numerical simulation

effects are considered in the numerical simulation, whereas the analytical model is based on the small deformation hypothesis. As the value (l_1/h) of cosine beam system decreases, the nonlinear behavior of numerical simulation will come closer to the experimental result.

The boundary condition used in the simulation also affects the performance of the metastructure, as the left and right edges of the metastructure are constrained in all directions, which is practically challenging. In the experiment, when the load is applied on the top of the metastructure, the left and right edges of the metastructure resist the deformation of the cosine beam system in a horizontal direction as the stiffness walls are fabricated using PLA. But this resistance was not sufficient to withstand the deformation of the cosine beam; this leads to the asymmetrical buckling of the cosine beam (as shown in Fig. 17c). This deleterious effect causes the slight mismatching of the numerical and experimental results in the quasi-zero stiffness region.

Thus, the results verify that a metastructure can be effectively designed to possess the quasi-zero stiffness mechanical behavior using the designing procedure

mentioned in this work for various vibration isolation applications.

4 Dynamic analysis

The vibration isolation property of metastructure is investigated based on the mechanical characteristics obtained in the static analysis. The static characteristics results reveal that the mechanical behavior of metastructure under vertical displacement contains three regions as obtained in Fig. 16, showing two approximate linear stiffness regions I and III and one quasi-zero stiffness region II. An object that needs to be isolated from the vibration is kept on the top surface of the metastructure, and its weight is majorly supported in region I. The quasi-zero stiffness region II is used to isolate the unwanted vibrations that act on the metastructure. The vibration isolation characteristics of the metastructure are investigated in this section.

The most important parameter used to measure vibration performance is transmissibility. The vibration isolation problems are categorized in two ways [16]: (a) force transmissibility problem, here the

exciting force is applied on the body kept at the top of the vibration isolation system, and the aim is to minimize the force transmitted to the base of the system; (b) motion transmissibility, here the base of the vibration isolation system is excited, and the main aim is to minimize the disturbance of the body kept at the top of the isolation system. Motion transmissibility problem studied in this work is consistent with the type of excitations applied in the analysis.

4.1 Frequency response curve

The equation of motion for the harmonic base excitation is given by

$$m\ddot{Y} + c\dot{Y} + F_{QZS}(Y) = -m\ddot{Z} \tag{41}$$

where Y is the relative displacement between the base and the isolated mass. $\ddot{Z}$ is the excitation acceleration applied at the base of the system and is assumed to be $\ddot{Z} = Z_0 \cos(\omega t)$. Equation (41) can be non-dimensionalized by introducing certain constants and variables:

$$\omega_n = \sqrt{\frac{k_v}{m}}, \quad \xi = \frac{c}{2m\omega_n}, \quad z_0 = \frac{Z_0}{\omega_n^2 L_0},$$
$$\Omega = \frac{\omega}{\omega_n}, \quad \tau = \omega_n t, \quad y = \frac{Y}{L_0} \tag{42}$$

where ω_n is the natural frequency of equivalent linear isolator, z_0 is the non-dimensional excitation acceleration amplitude, y is the non-dimensional relative displacement, Ω is the non-dimensional frequency ratio, ξ is the damping ratio, and τ is the non-dimensional time. The equation of motion (mentioned in Eq. 41) can be written in non-dimensional form as

$$y'' + 2\xi y' + \alpha y^3 + \delta y^5 = -z_0 \cos(\Omega\tau) \tag{43}$$

where a prime ($'$) denotes the non-dimensional time derivative τ, ξ is the damping ratio, α is the coefficient of third-order dimensionless displacement, and δ is the coefficient of fifth-order dimensionless displacement. The damping ratio ξ influences the amplitude and transmissibility of the system, and it also affects the jump phenomenon, which is the basic threshold for effective isolation. In this study, the value of the non-dimensional parameter α is always positive (represents hardening), which leads to the bending of the frequency response curve to the right, as presented in [45]. The non-dimensional parameter δ reduces the bending of the frequency response curve and therefore

helps in increasing the effective isolation range of the system. Equation (43) is the approximate dynamic equation, which under small-amplitude excitation expresses the steady-state vibration of the isolated system around the static equilibrium position. Equation (43) can be referred to as a nonlinear dynamic equation.

The solution of Eq. (43) comprises two parts: The first is a particular solution, and the second is the free vibration term. The damping considered in this work is positive, so the free vibration term dies away with time. The method used in this work to find the steady-state response of the vibration system is harmonic balance (HB) method. The merits and demerits of the HB method are explained in [46].

The single-mode HB approximation can be represented as

$$y(\tau) = A\cos(\Omega\tau + \phi) \tag{44}$$

where ϕ is the phase response and A is the amplitude, and the first and second derivative of single mode can be represented as

$$y'(\tau) = -A\Omega\sin(\Omega\tau + \phi) \tag{45}$$

$$y''(\tau) = -A\Omega^2\cos(\Omega\tau + \phi) \tag{46}$$

Substituting Eqs. (44), (45), and (46) into Eq. (43) and ignoring the third and fifth harmonic, we obtain

$$-\Omega^2 A + \left(\frac{3}{4}\alpha A^3\right) + \left(\frac{5}{8}\delta A^5\right) = -z_0\cos(\phi) \tag{47a}$$

$$-2\xi A\Omega = -z_0\sin(\phi) \tag{47b}$$

On squaring Eqs. (47a) and (47b), and adding afterward, Eq. (48) can be obtained by eliminating ϕ (elaborated in "Appendix E")
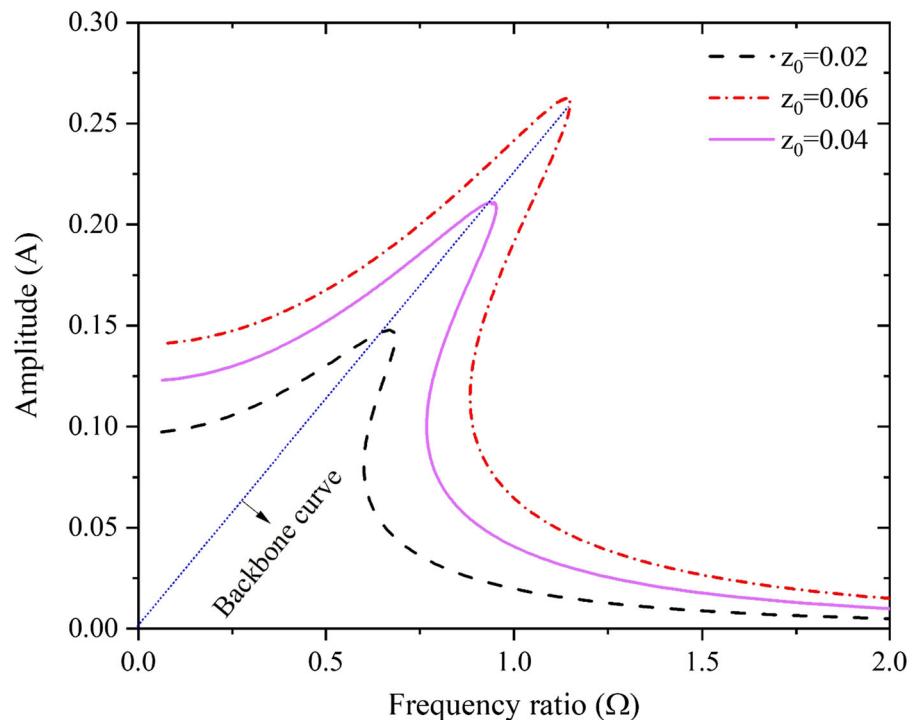
$$\frac{25}{64}\delta^2 A^{10} + \frac{15}{16}\delta\alpha A^8 + \left(\frac{9}{16}\alpha^2 - \frac{5}{4}\Omega^2\delta\right)A^6 - \frac{3}{2}\Omega^2\alpha A^4$$
$$+ \left[\Omega^4 + (4\xi^2\Omega^2)\right]A^2 - z_0^2 = 0 \tag{48}$$

or

$$\Omega_{1,2} = \pm\left\{ \begin{array}{c} \left[\left(-\frac{5}{8}\delta A^4 - \frac{3}{4}\alpha A^2 + 2\xi^2\right)^2 - \left(\frac{25}{64}\delta^2 A^8 + \frac{15}{16}\delta\alpha A^6 + \frac{9}{16}\alpha^2 A^4 - \frac{z_0^2}{A^2}\right)\right]^{\frac{1}{2}} \\ + \left(\frac{5}{8}\delta A^4 + \frac{3}{4}\alpha A^2 - 2\xi^2\right) \end{array} \right\}^{\frac{1}{2}} \tag{49}$$

Solving the above equation gives the steady-state response amplitude. The frequency response plot is shown in Fig. 19 for varying excitation amplitudes with constant damping ratio and in Fig. 20 for varying damping ratio and constant excitation amplitude. The frequency response (FR) curve shows a trend of bending to the right; this happens because of the positive nonlinear coefficient α, which makes this system attributed to the hardening stiffness case. The bending of the FR curve causes a jump in the amplitude of the system when the excitation frequency is swept either from left to right or right to left; this phenomenon is referred to as the jump frequency phenomenon. It can be observed from Fig. 19 that increasing the excitation amplitude causes an increase in the peak response amplitude and peak response frequency and thus aggravates the jump phenomenon, whereas Fig. 20 shows a decrease in peak resonance amplitude and peak resonance frequency with the increased damping ratio, thus suppressing the jump phenomenon.

4.2 Analysis for the peak response

The response amplitude obtained in Eq. (48) is expressed in the form of a quadratic equation of Ω^2. Here, Ω_1 and Ω_2 can be seen as the abscissae of the amplitude–frequency curve's two intersections, as shown in Figs. 19 and 20. At the peak resonance point, both the intersections coincide with each other, i.e., Ω_1 became equal to Ω_2. Thus, the nested square root of Eq. (49) becomes zero, leading to a relation for the peak resonance amplitude (denoted as A_p) (elaborated in "Appendix F").
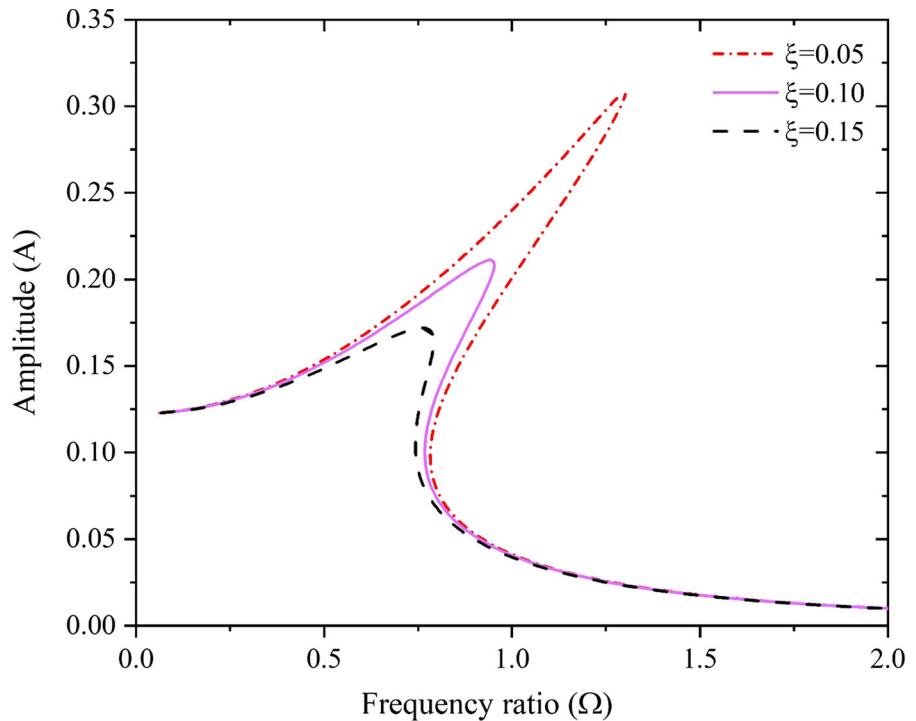
$$\frac{5}{2}\delta A_p^6 + 3\alpha A_p^4 - 4\xi^2 A_p^2 - \frac{z_0^2}{\xi^2} = 0 \tag{50}$$

The value of frequency ratio at which the peak resonance (Ω_p) occurs is given by
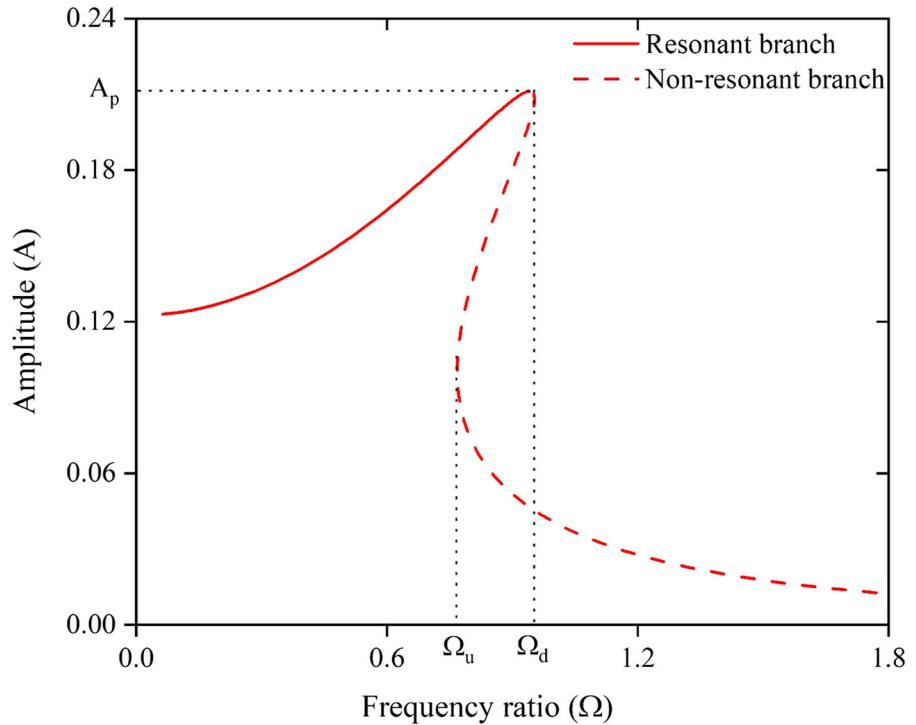
$$\Omega_p = \sqrt{\frac{5}{8}\delta A_p^4 + \frac{3}{4}\alpha A_p^2 - 2\xi^2} \tag{51}$$

A frequency response curve is plotted in Fig. 21 for $z_0 = 0.04$, $\zeta = 0.10$, and $\gamma = 0.5$. In this case, firstly, the value of peak resonance amplitude (Ap) is calculated. Then, varying values of A from (0 to Ap) are substituted in Eq. (49) to obtain the corresponding


Fig. 19 Frequency response curve under varying excitation amplitude when $\zeta = 0.10$ and $\gamma = 0.5$

Fig. 20 Frequency response curve for varying damping ratio when $z_0 = 0.04$ and $\gamma = 0.5$

Fig. 21 Frequency response curve showing the peak response (A_p), jump-up frequency (Ω_u), and jump-down frequency (Ω_d) for $z_0 = 0.04$, $\zeta = 0.10$, $\gamma = 0.5$

values of Ω_1 and Ω_2. As A is varied from 0 to A_p, it shows the jump phenomenon that characterizes the forced response of a Duffing oscillator [47].

The frequency response plot in Fig. 21 can be observed in two ways: (i) When Ω increases from 0, the value of A increases following the upper branch, referred to as resonant branch until the peak response amplitude (A_p). The value of Ω at A_p corresponds to jump-down frequency Ω_d; any further increase in Ω causes the response to jump to a lower curve, also known as a non-resonant branch [48]. (ii) When Ω decreases (in the limit from infinity), resonance amplitude A follows the non-resonant branch until the jump-up frequency Ω_u. A further decrease in Ω causes a sudden jump of the response to the resonant branch.

As discussed earlier in Figs. 19 and 21, the peak of response amplitude A and excitation frequency ratio Ω are both increased by increasing excitation amplitude z_0 and decreasing damping ratio ζ. Therefore, it is necessary to find the limiting value of excitation amplitude z_0 applied to the base of the system to achieve the peak resonance at $\Omega > 0$. However, if z_0 is too small or ζ is too large, then the frequency response curve may become a monotonic decreasing function with no peak response but the only maximum response at $\Omega = 0$. The critical value of peak response A_p that makes the frequency response curve monotonically decreasing is achieved by equating Eq. (51) to zero. Solving $\Omega_p = 0$ gives

$$A_p^2 = \frac{1}{\delta}\left(\sqrt{\frac{9}{25}\alpha^2 + \frac{16}{5}\delta\xi^2} - \frac{3}{5}\alpha\right) \tag{52}$$

By substituting Eq. (52) into Eq. (50), the limiting value of excitation amplitude is achieved for the disappearance of peak resonance:

$$z_0 = 2\xi^2\sqrt{\frac{1}{\delta}\left(\sqrt{\frac{9}{25}\alpha^2 + \frac{16}{5}\delta\xi^2} - \frac{3\alpha}{5\delta}\right)} \tag{53}$$

If the value of z_0 is larger than that given in Eq. (53), peak resonance exists. If z_0 is smaller, then the frequency curve monotonically decreases, and thus there is no peak, and the maximum response occurs at $\Omega = 0$.

4.3 Motion Transmissibility

Transmissibility is one of the most important parameters for measuring the performance of a vibration isolator. Motion transmissibility is defined as the ratio of the magnitude of absolute displacement at the isolated mass to the absolute displacement at the base. Since, in this case, the base of the system and isolated mass excite at the same frequency, the expression of acceleration amplitude can be directly used here to give the definition of motion transmissibility:
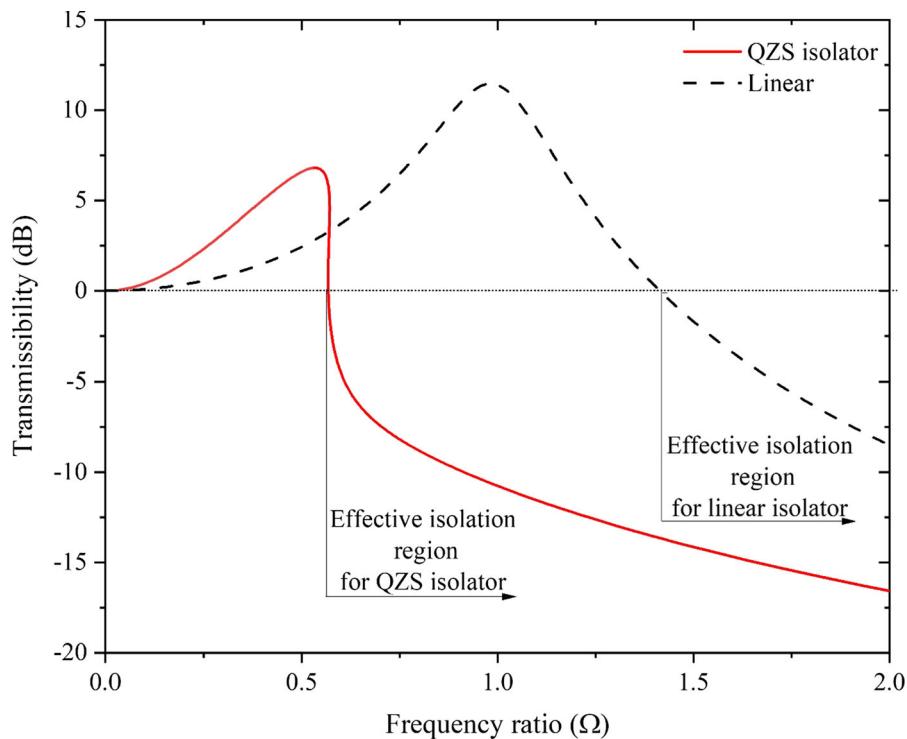
$$\begin{aligned} T &= \frac{|z_0\cos(\Omega\tau) + y''|}{z_0} \\ &= \frac{\sqrt{(\Omega^4 A^2) - (2\Omega^2 A z_0\cos\phi) + z_0^2}}{z_0} \end{aligned} \tag{54}$$

Substituting the value of $\cos(\varphi)$ from Eq. (47a) (elaborated in "Appendix G"),
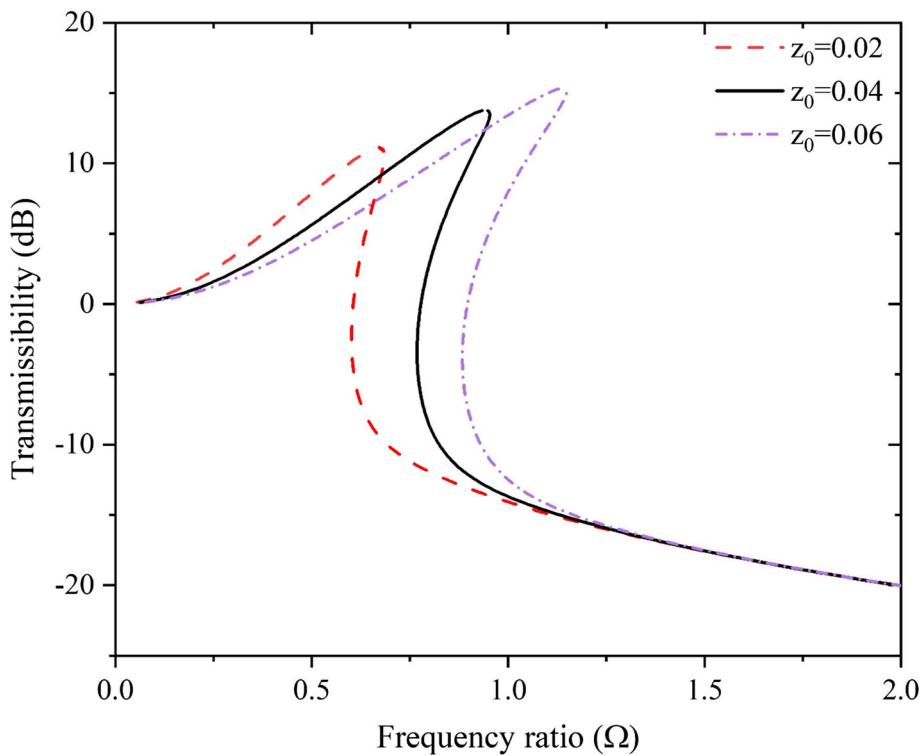
$$T = \sqrt{\left(\frac{\Omega A}{z_0}\right)^2\left(\frac{5}{4}\delta A^4 + \frac{3}{2}\alpha A^2 - \Omega^2\right) + 1} \tag{55}$$

The value of transmissibility is obtained by substituting the relation between A and Ω obtained in Eq. (49). For a given system under any excited amplitude, the transmissibility varies with the excitation frequency. So, the plot between transmissibility and excitation frequency ratio is used here to characterize the performance of the proposed system. The transmissibility–frequency plot in Fig. 22 shows the comparison between the QZS isolator and the linear isolator. It can be observed that the peak transmissibility of the QZS isolator is less than that of the linear one, and also, QZS has a much wider isolation range than the linear one.

A parametric study is performed showing the influence of different parameters on the transmissibility curves. Figure 23 shows the influence of different excitation amplitudes on transmissibility; it can be observed that with the increase in the amplitude excitation, the peak transmissibility increases, and the effective isolation range decreases. Figure 24 shows the influence of different damping ratios on the transmissibility; it can be observed that with the increase in the damping ratio, the peak frequency and peak transmissibility decrease, and also the effective isolation range is observed to be high for the high damping ratio. However, for the low damping case, we
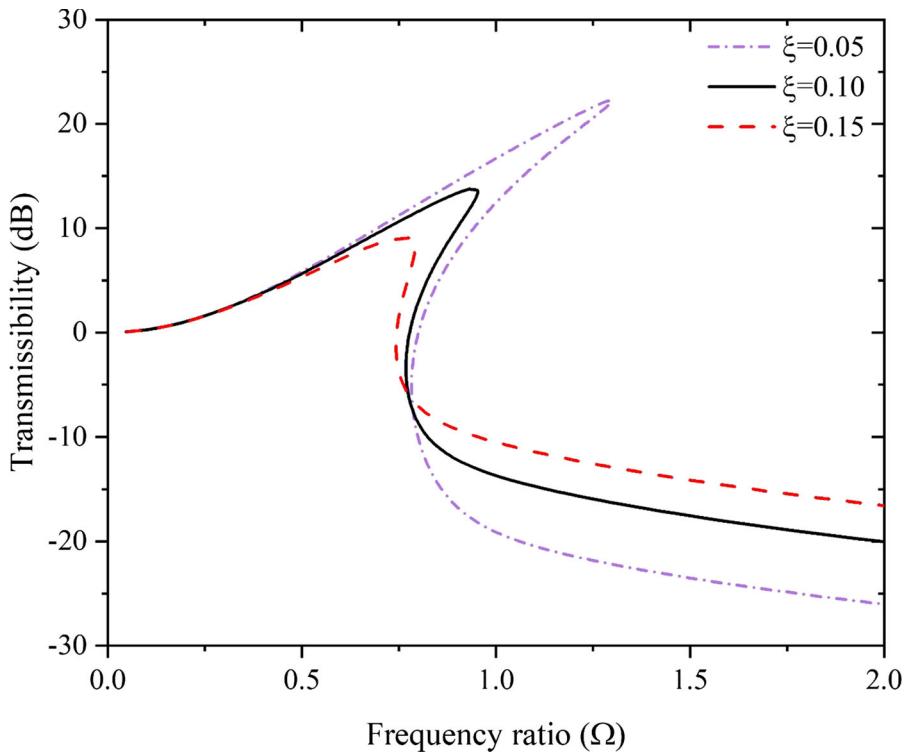
Fig. 22 Transmissibility curve showing a comparison between QZS and linear isolator when $z_0 = 0.02$, $\zeta = 0.1$, $\gamma = 0.5$

Fig. 23 Transmissibility curve under different excitation amplitudes when $\zeta = 0.1$ and $\gamma = 0.5$

Fig. 24 Transmissibility curve under different damping ratios when $\gamma = 0.5$

can achieve lower transmissibility for the same frequency ratio compared to the higher damping ratio. Finally, it can be summarized that small-amplitude excitation and appropriate damping can be considered for good overall isolation performance.

Peak transmissibility is an important parameter for measuring isolation performance. It can be seen that the transmissibility reaches its peak value at the peak resonance. The peak transmissibility can be approximated by substituting values A_p (Eq. 52) and Ω_p (Eq. 51) into the equation of transmissibility (Eq. 55):

$$T_p = \sqrt{\frac{A_p^2}{z_0^2}\left[\left(\frac{5}{8}\delta A_p^2 + \frac{3}{4}\alpha\right)^2 A_p^4 - 4\xi^4\right] + 1} \qquad (56)$$

4.4 Numerical simulation

Motion transmissibility is one of the most prominent parameters to evaluate the performance of vibration isolators at the steady state for each of the certain frequency ranges. In this subsection, finite element analysis is carried out to simulate the vibration performance of the metastructure by using

commercial ANSYS R19 software. The time response of the QZS model is studied numerically, and the transmissibility of the QZS system at the steady state is predicted for each of the given excitation frequencies, and further, the results are validated with the analytical values. The metastructure is assumed to support a mass on its top surface; the mass is designed in such a way that it should be supported by the approximate linear stiffness region I (shown in Fig. 16) so that the isolation performance can be achieved in the QZS region II.

The proposed model of metastructure with a mass assumed to be kept on its top surface is subjected to a sinusoidal wave excitation $z = 2.10\sin(\omega t)$ at its base, where 2.10 m/s^2 is the amplitude of excitation acceleration, ω is the excitation frequency, and t is the time range in seconds. The time response of the metastructure in terms of absolute acceleration for various excitation frequencies with constant damping coefficient ($\zeta = 0.15$) is shown in Fig. 25, where the red line represents the response at the top of the mass and the black dotted line represents the response of sinusoidal excitation at the base. It can be observed that with the increase in excitation frequency, the response of the proposed metastructure is increased as compared to

the base excitation sinusoidal input as the system approaches peak response. A further increase in excitation frequency results in a remarkable reduction in the response as the system approaches the effective isolation range.

The root-mean-square (RMS) value of the acceleration response is calculated for all the obtained time responses. Further, the approximate motion transmissibility can be calculated for each time response based on the RMS values as

$$T = 20 \log_{10}\left(\frac{\text{TOP}_{\text{RMS}}}{\text{BOTTOM}_{\text{RMS}}}\right) \tag{57}$$

A frequency response curve is then plotted from the calculated transmissibility values against their respective frequency ratios (obtained from the excitation frequency). The numerically obtained results are compared with the analytical results obtained from Eq. (55) with the following parameters ($z_0 = 0.05$, $\zeta = 0.15$, $\gamma = 0.5$). As shown in Fig. 26, the numerical results are in good agreement with the analytical solutions. Some variation can be seen in the analytical and numerical results, and this might be due to the approximation introduced by HBM used to solve the dynamic equation analytically.

It is understood that a superior isolator possesses lower transmissibility with a wide effective isolation range. As it can be seen in Fig. 26 that, with the increase in excitation frequency, the transmissibility first increases till it achieves the resonance peak, then it starts decreasing with the further increase in the excitation frequency. In the proposed QZS system, the peak response occurs at 14 Hz with a transmissibility of 9.5 dB, whereas the effective isolation range means that the transmissibility of the system is lesser than zero, ensuring that the displacement amplitude at the top of the isolated object is lesser than that of the base. It can be observed that the effective isolation range of the QZS model starts from 16 Hz with the transmissibility of − 1.6 dB, and the suppression of vibration transmission is enhanced with the further increase in the excitation frequency after 16 Hz. Therefore, the proposed model can be effectively used for low frequency as its natural frequency is lesser than that of the linear counterpart, and also, QZS has a larger effective isolation range than that of the linear one.

A simulation is performed to study the effect of damping coefficient on the transmissibility of the QZS model under sinusoidal base excitation. Three different damping coefficients are studied under the same vibration excitation frequency. Two different sets of excitation frequencies are applied, and their time response is shown in Fig. 27.

The root-mean-square (RMS) value of the acceleration response is calculated for all the obtained time responses. Further, the approximate motion transmissibility is calculated from Eq. (57) and plotted in Fig. 28. It can be observed that for the excitation frequency lying outside the effective isolation range, the transmissibility of the QZS structure increases with the increase in the damping ratio. But for the excitation frequency lying in the effective isolation range, the transmissibility decreases with an increase in the damping coefficient. This indicates that the QZS structure with a small damping coefficient will give better isolation performance.

5 Stability of the steady-state response

A system whose structural response changes abruptly due to a small change in one of its parameters is known as structurally unstable. In this section, the stability analysis is performed to identify the unstable region of the proposed model. As the steady-state behavior of the QZS model is obtained using the HB method, the same will be used for identifying the stability of that response. The stability is investigated by introducing a small dimensionless perturbation $\epsilon(\tau)$ and superposing it in Eq. (44) as

$$y(\tau) = A\cos(\Omega\tau + \phi) + \varepsilon(\tau) \tag{58}$$
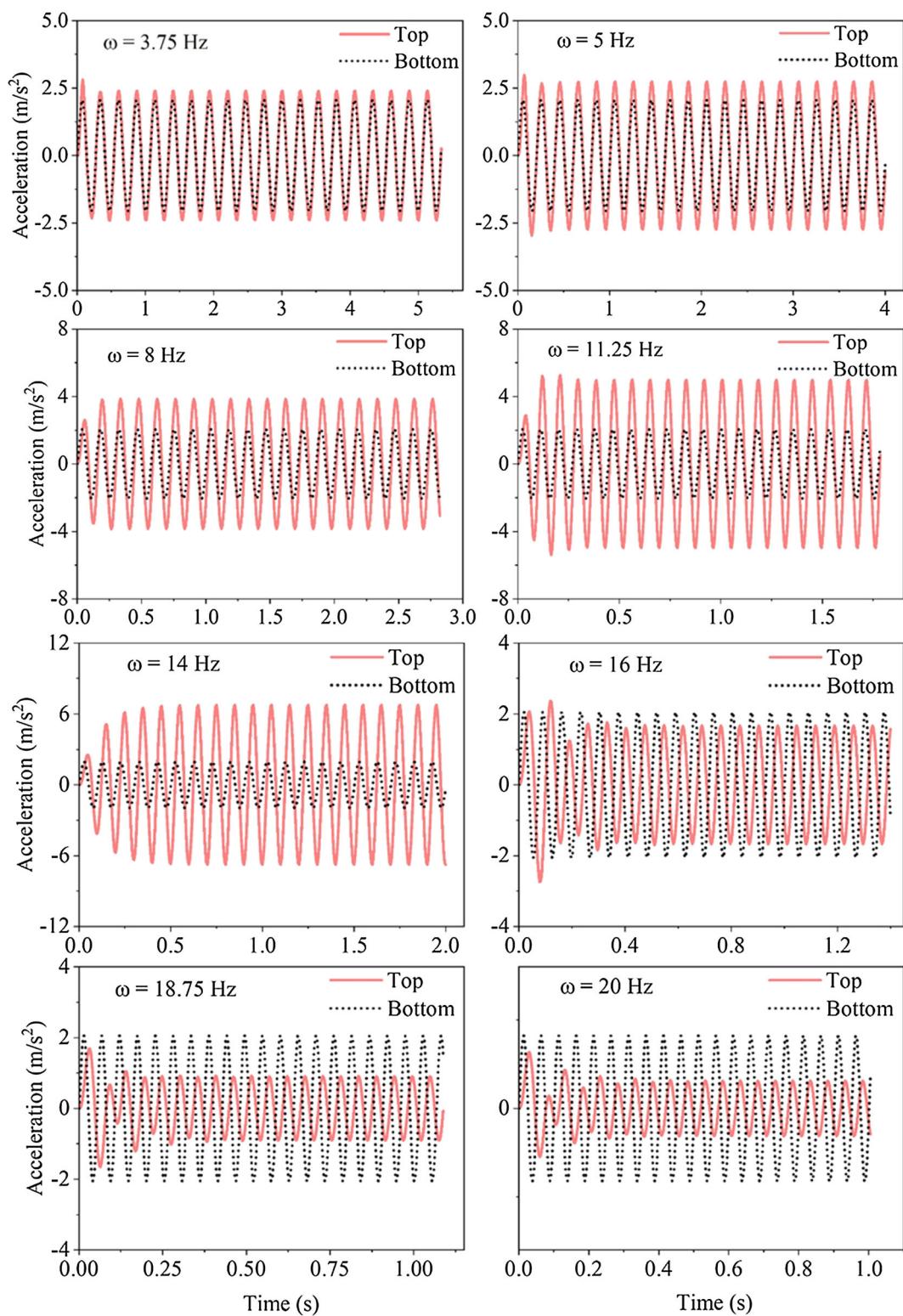
By substituting Eq. (58) into Eq. (43), and neglecting the terms of order higher than those $O(\epsilon^2)$ and higher-order harmonics in the response, the motion of the system is expressed in terms of dimensionless perturbation as

$$\varepsilon'' + 2\mu\varepsilon' + (p - 2q\cos 2\theta)\varepsilon = 0, \tag{59}$$
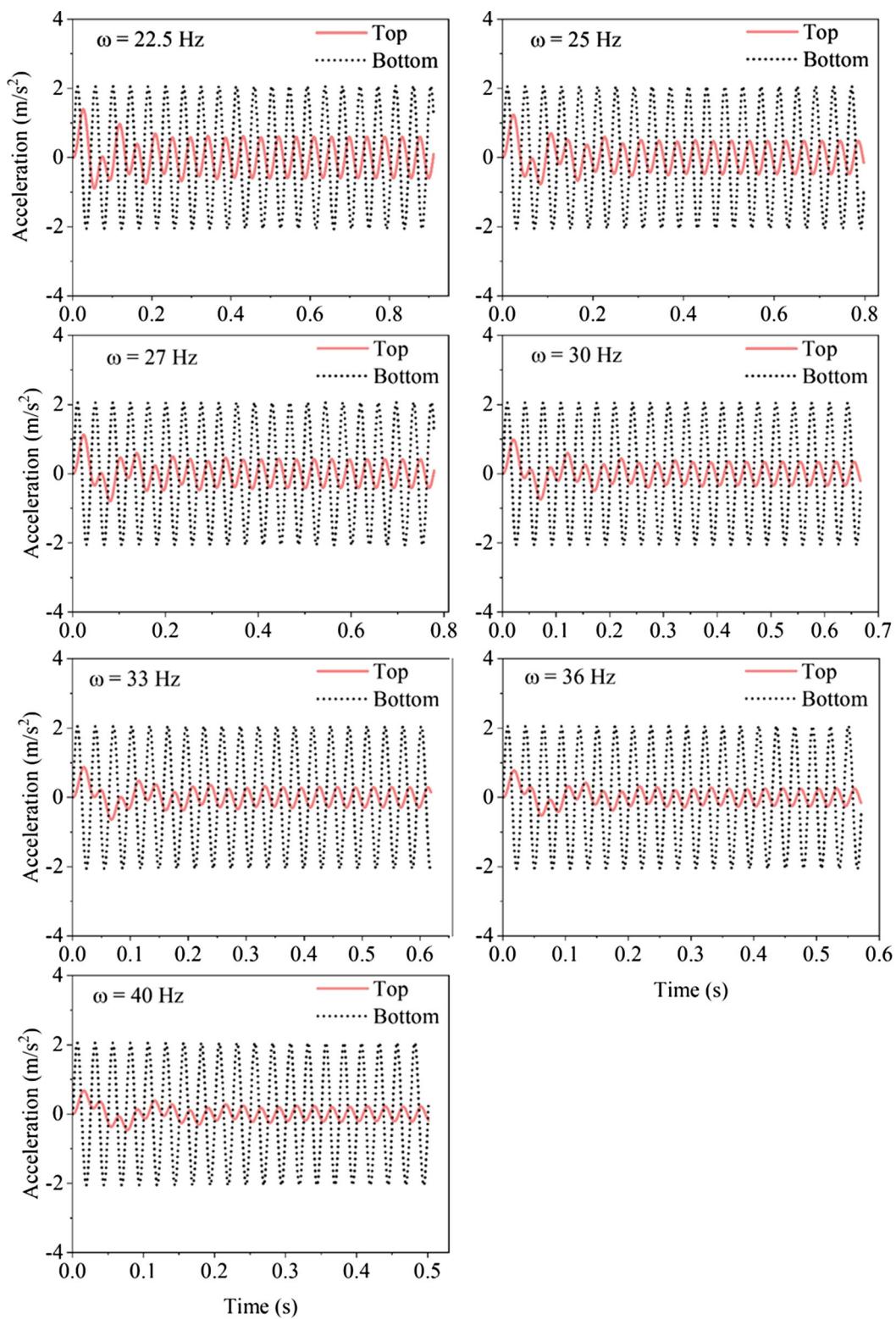
letting

$$p = \frac{3\alpha A^2}{2\Omega^2}, \quad q = -\frac{3\alpha A^2}{4\Omega^2}, \quad \mu = \frac{\xi}{\Omega} \tag{60}$$

Equation (59) is known as damped Mathieu's equations [49]. Here, p is a function of q that represents the transition curve that separates the pq
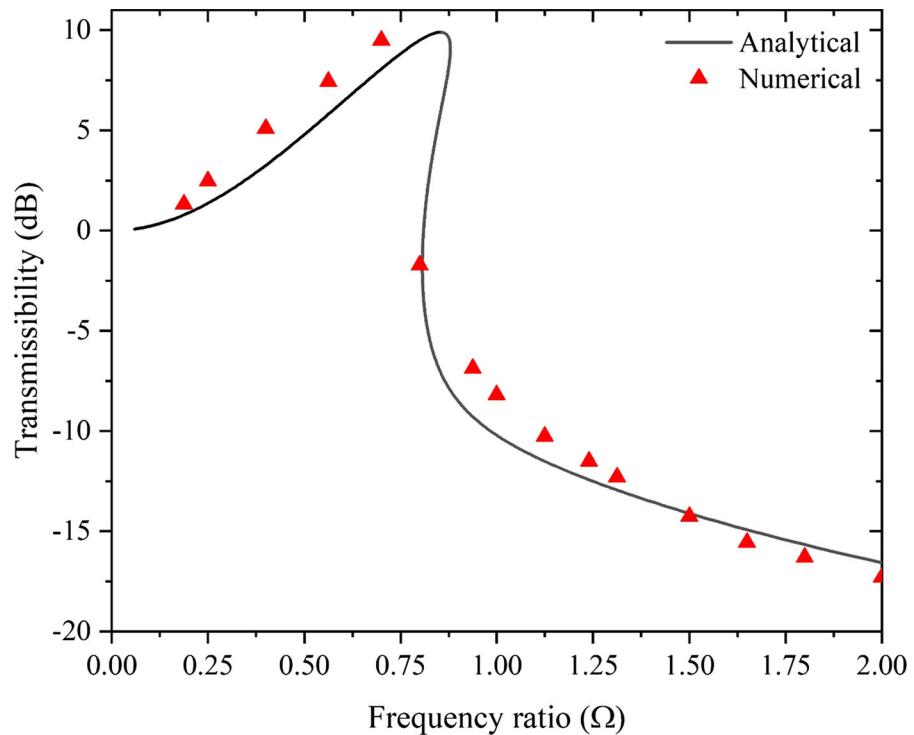
Fig. 25 Time response of the metastructure under different excitation frequencies, when $\zeta = 0.15$ and $\gamma = 0.5$

Fig. 25 continued

Fig. 26 Comparison between the numerical and analytical transmissibility curve

plane into stable and unstable regions. Nayfeh et al. [50] performed a perturbation analysis to obtain the leading term approximation of the transition curve obtained in Eq. (59). The solution of Eq. (59) is unstable if it lies outside the parabola,

$$p = 1 \pm \sqrt{q^2 - 4\mu^2} \qquad (61)$$

By substituting values of Eq. (60) into Eq. (61), the unstable region is found to be enclosed by the curves (elaborated in "Appendix H"),

$$\Omega_{us1} = \sqrt{\frac{3}{2}\alpha A^2 - 2\xi^2 + \frac{1}{2}\sqrt{\left(4\xi^2 - 3\alpha A^2\right)^2 - \frac{27}{4}\alpha^2 A^4}}$$
(62a)
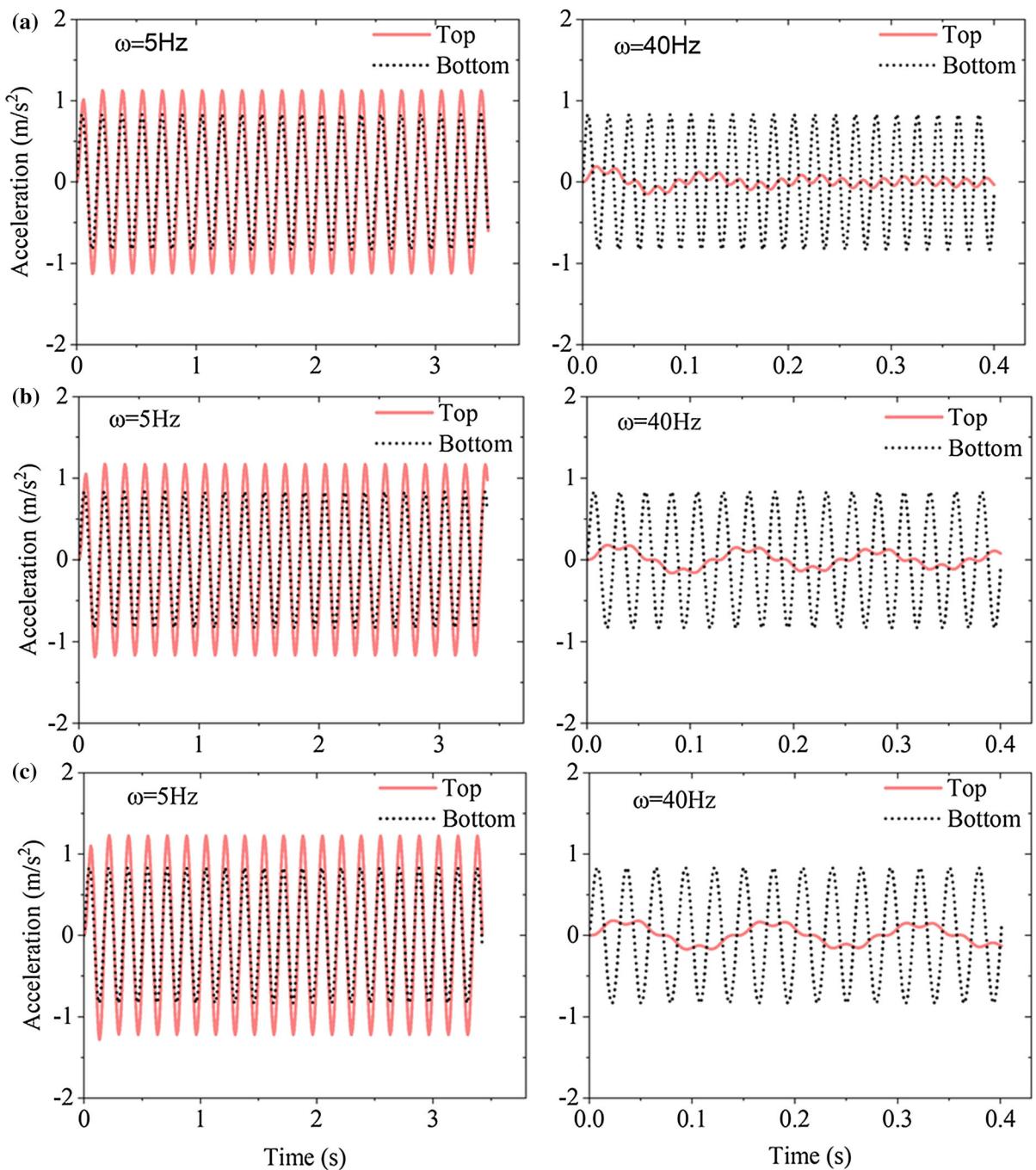
$$\Omega_{us2} = \sqrt{\frac{3}{2}\alpha A^2 - 2\xi^2 - \frac{1}{2}\sqrt{\left(4\xi^2 - 3\alpha A^2\right)^2 - \frac{27}{4}\alpha^2 A^4}}$$
(62b)

Equation (62a) and (62b) is plotted in Fig. 29 under the same parameter of Fig. 21. The unstable region can be observed inside the shaded area. It can be observed that whenever there is bending in the FR curve, the jump phenomenon occurs, and the intermediate branch nearby the bending of the frequency response curve is unstable. This unstable intermediate branch of the FR curve always lies between the jump-up and jump-down frequencies, as can be observed in Fig. 29. Thus, the value of jump-up and jump-down frequencies can also be calculated at the intersection of the FR curve and the stability boundary. A parametric study is performed for studying the behavior of the stability curve; it can be observed from Fig. 30 that the unstable region gets reduced by increasing the damping ratio and is independent of the applied excitation amplitude.

6 Conclusion

The concept of obtaining quasi-zero stiffness is proposed in this work by combining the negative stiffness element in parallel with the positive stiffness elements. The static characteristics and dynamic behavior of the proposed model are considered. Then, using the design procedure, a metastructure is designed to obtain high static and low dynamic stiffness (HSLDS).
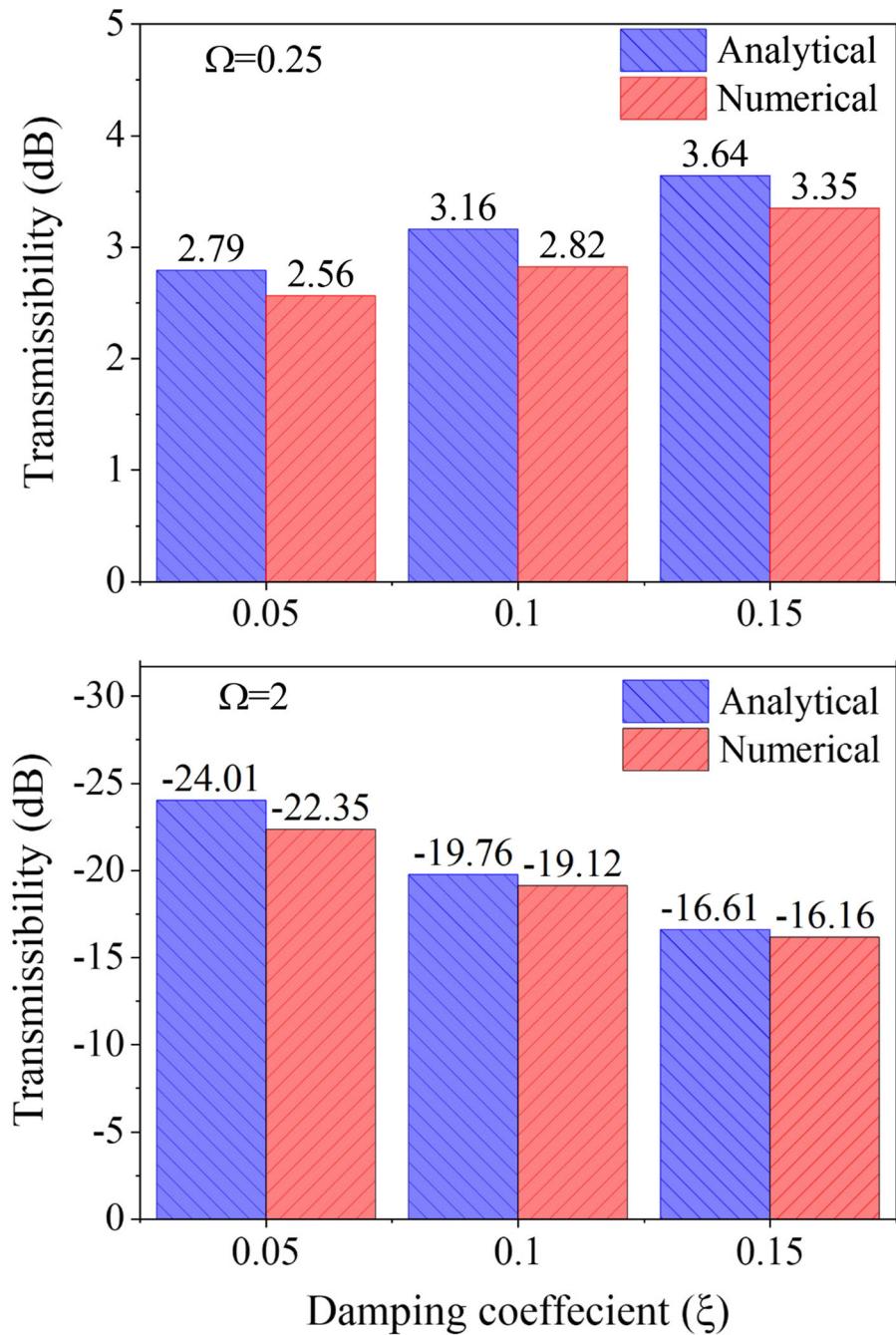
Fig. 27 Time response of the metastructure for three different damping coefficients: **a** $\zeta = 0.05$, **b** $\zeta = 0.1$, **c** $\zeta = 0.15$, when amplitude of applied acceleration is 0.85 m/s^2

The proposed metastructure is the parallel arrangement of a four-unit cell, where the unit cell is constructed using the parallel arrangement of one cosine beam system and two semicircular arches.

Under the transverse load, the cosine beam system experiences a snap-through behavior and possesses negative stiffness between two stable states, whereas, under vertical load, the bending-dominated
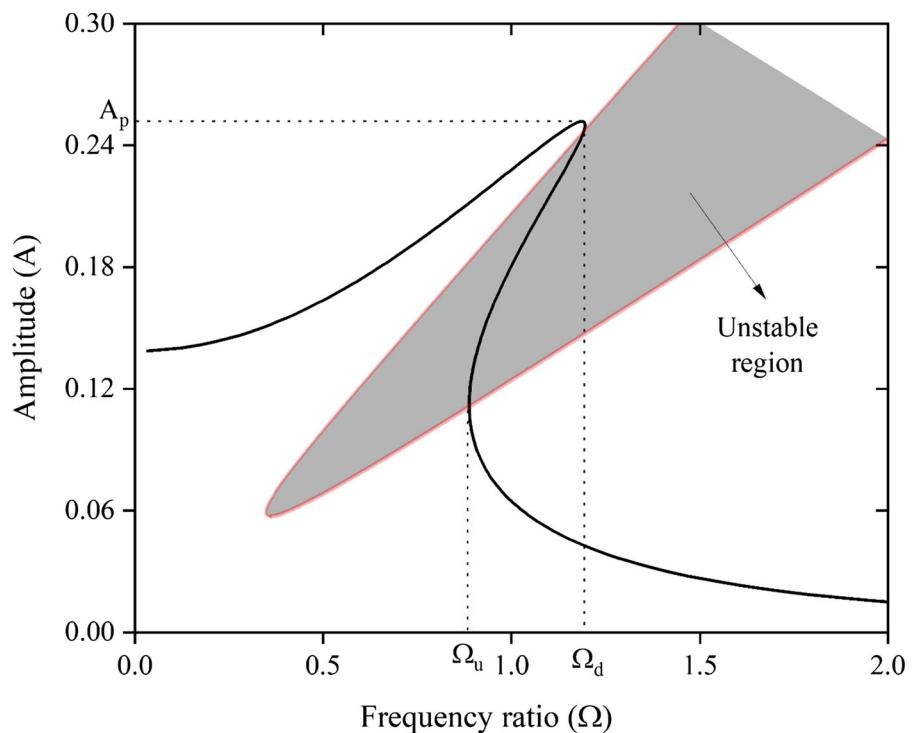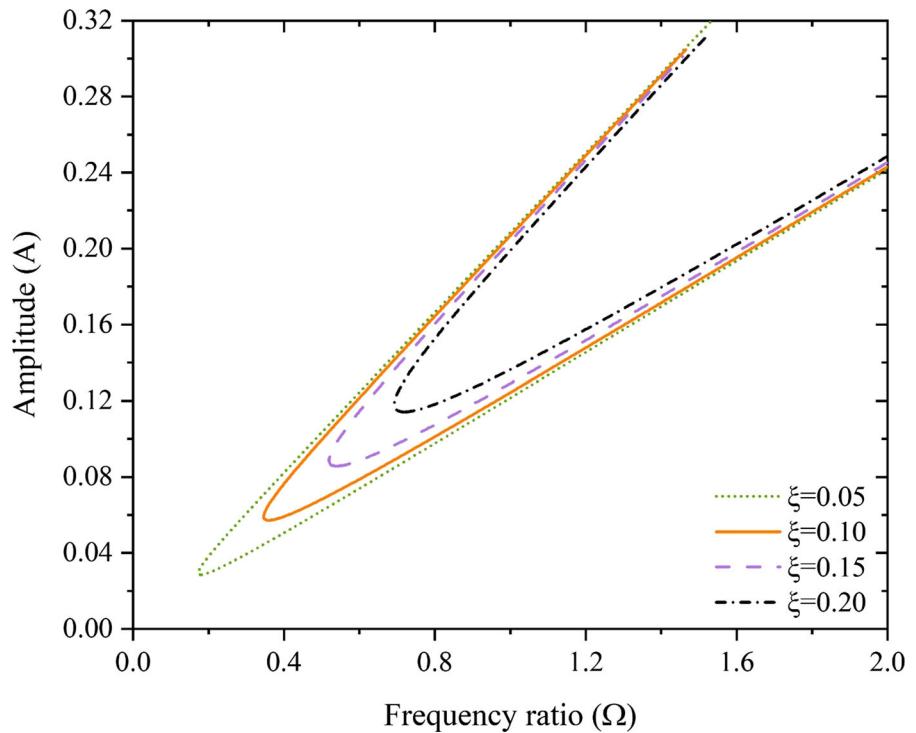
semicircular arches possess positive stiffness. Thus, the combination of this negative and positive stiffness leads to a quasi-zero stiffness region for a certain amount of vertical displacement. The force–displacement relation of the metastructure is derived analytically and approximated using the fifth-order Taylor equation. Further, the force–displacement curve is studied for various values of stiffness ratio and geometrical parameters to obtain the quasi-zero-stiffness behavior. An experiment is performed to study the force–displacement characteristics of the metastructure that showed a QZS region and two approximate linear regions. In addition, a finite element analysis is performed using simulating software to

Fig. 29 Unstable region in the (A, Ω) plane, when $\gamma = 0.5$ and $\zeta = 0.10$

Fig. 30 Unstable region in the (A, Ω) plane for different damping ratio values, when $\gamma = 0.5$

study the QZS behavior. Finally, the analytical and numerical results come in good agreement with the experimental results.

This work considered forced vibration of the proposed model under harmonic base excitation to study the dynamic behavior. The approximate nonlinear dynamic equation is obtained. The harmonic balance method (HBM) is employed for solving the nonlinear dynamic equation to obtain the response of the system for each of the given excitation frequencies. The results of the frequency response curve are used for obtaining the motion transmissibility with respect to the excitation frequency. Further, the time response of the system is also studied under sinusoidal base excitations. The simulation results show that lower transmissibility and wider effective isolation range are obtained by the proposed QZS metastructure compared to the equivalent linear model. The parametric study shows that the motion transmissibility increases with increasing damping ratio in the effective isolation range, indicating that the metastructure with a small damping coefficient and higher frequency ratio will possess better vibration isolation performance. The stability analysis indicated an unstable region between the jump-up and jump-down frequency in the frequency response curve. It can also be observed that the unstable region reduces with an increase in the damping ratio, and stability is independent of the applied excitation amplitude. Based on all the analysis and parametric studies, the proposed design is suitable for the low-frequency vibration reduction in microdevices, precision instruments, and lightweight devices.

Data availability The datasets generated during and/or analyzed during the current study are available from the corresponding author on reasonable request.

Declarations

Appendix

A. Derivation of Eq. (27)

Substituting the static equilibrium condition ($x = 0$) in Eq. (25) and equating k_{QZS} to zero

$$k_{QZS}(x) = 8 + 4\mu - \frac{4\mu\gamma^2}{(\gamma^2 + x^2)^{3/2}} \tag{25}$$

$$0 = 8 + 4\mu - \frac{4\mu\gamma^2}{(\gamma^2 + 0)^{3/2}} \tag{63}$$

$$0 = 8 + 4\mu - \frac{4\mu\gamma^2}{\gamma^3} \tag{64}$$

$$0 = 8 + 4\mu\left(1 - \frac{1}{\gamma}\right) \tag{65}$$

$$\mu\left(1 - \frac{1}{\gamma}\right) = -2 \tag{66}$$

$$\mu_{QZS} = \frac{-2\gamma}{\gamma - 1} = \frac{2\gamma}{1 - \gamma} \tag{67}$$

$$\text{or,} \quad 0 = 8 + 4\mu\left(1 - \frac{1}{\gamma}\right) \tag{65}$$

$$\mu\left(1 - \frac{1}{\gamma}\right) = -2 \tag{68}$$

$$-\frac{1}{\gamma} = \frac{-2}{\mu} - 1 \tag{69}$$

$$\frac{1}{\gamma} = \frac{2}{\mu} + 1 \tag{70}$$

$$\gamma_{QZS} = \frac{\mu}{\mu + 2} \tag{71}$$

$$\mu_{QZS} = \frac{2\gamma}{1 - \gamma} \quad \gamma_{QZS} = \frac{\mu}{\mu + 2}. \tag{27}$$

B. Dependence of geometrical parameter (γ) and stiffness parameter (μ)

Based on Eq. (25), a study is performed to show the variation of k_{QZS} with x for different values of γ and μ based on the three different conditions:

$$k_{\text{QZS}}(x) = 8 + 4\mu - \frac{4\mu\gamma^2}{(\gamma^2 + x^2)^{3/2}} \tag{25}$$

$$\mu_{\text{QZS}} = \frac{2\gamma}{1 - \gamma} \quad \gamma_{\text{QZS}} = \frac{\mu}{\mu + 2} \tag{27}$$

B.i. Let's consider μ as some constant value to analyze the dependency of γ on Eq. (25).

Assume $\mu = 2$, then $\gamma_{\text{QZS}} = 0.5$ (from Eq. 27). Here, three different cases are discussed: (a) $\gamma = \gamma_{\text{QZS}} = 0.5$, (b) $\gamma = 0.6 > \gamma_{\text{QZS}}$, (c) $\gamma = 0.4 < \gamma_{\text{QZS}}$.

A curve is plotted in Fig. 31 based on Eq. (25) for comparing the three cases. It can be observed that for $\gamma = \gamma_{\text{QZS}}$, the equivalent stiffness is zero at the static equilibrium position ($x = 0$). For $\gamma < \gamma_{\text{QZS}}$, the equivalent stiffness becomes negative at static equilibrium position making the system unstable. For $\gamma > \gamma_{\text{QZS}}$, the equivalent stiffness becomes positive, and the QZS property is lost.

It can be observed that the system is unstable for the condition $\gamma < \gamma_{\text{QZS}}$.

B.ii. Let's consider γ as some constant value to analyze the dependency of μ on Eq. (25).

Assume $\gamma = 0.5$, then $\mu_{\text{QZS}} = 2$ (from Eq. 27). Here, three different cases are discussed: (a) $\mu = \mu_{\text{QZS}} = 2$, (b) $\mu = 2.5 > \mu_{\text{QZS}}$, (c) $\mu = 1.5 < \mu_{\text{QZS}}$.

A curve is shown in Fig. 32 based on Eq. (25) for comparing the three cases. It can be observed that for $\mu = \mu_{\text{QZS}}$, the equivalent stiffness is zero at the static equilibrium position ($x = 0$). For $\mu > \mu_{\text{QZS}}$, the equivalent stiffness becomes negative at static equilibrium position making the system unstable. For $\mu < \mu_{\text{QZS}}$, the equivalent stiffness becomes positive, and the QZS property is lost.

It can be observed that the system is unstable for the condition $\mu > \mu_{\text{QZS}}$.

B.iii. Equation (27) shows the relation between μ and γ, i.e.,
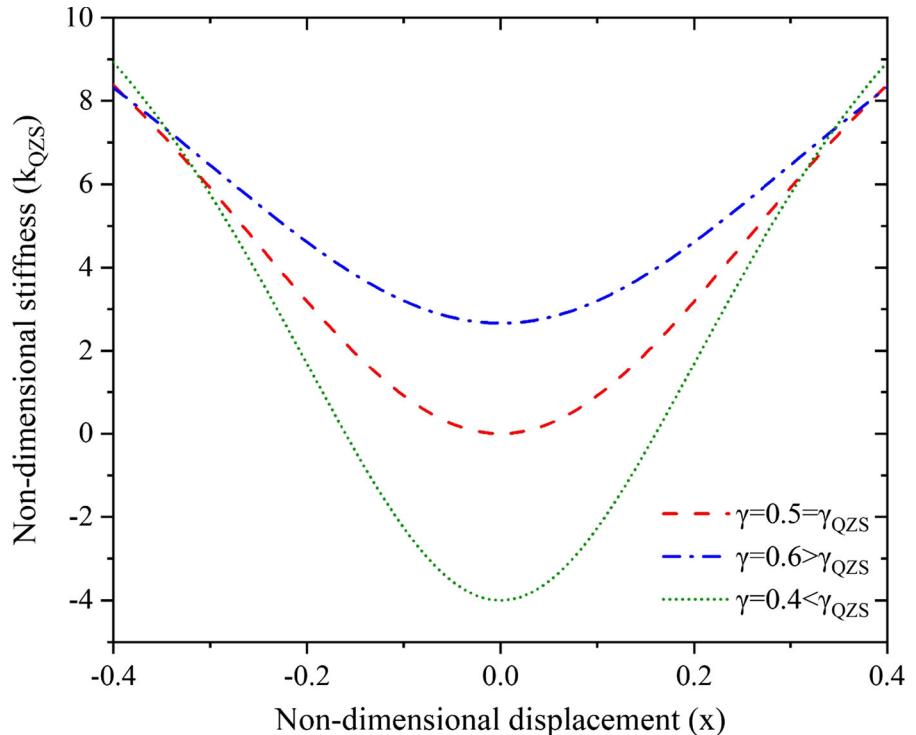
$$\mu_{\text{QZS}} = \frac{2\gamma}{1 - \gamma} \quad \gamma_{\text{QZS}} = \frac{\mu}{\mu + 2} \tag{27}$$

From Fig. 5a and Eq. (18), it can be observed that
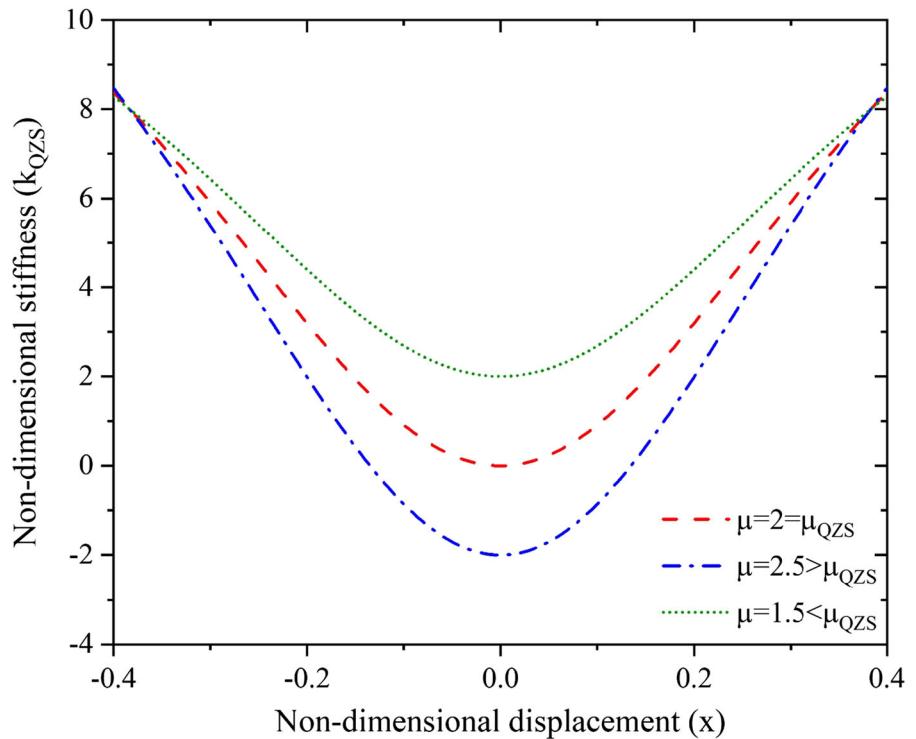
$$\gamma = \frac{L_1}{L_0} = \cos\theta \tag{72}$$

As it is known that the range of cosine varies from 0 to 1, the extreme values of γ are 0 and 1. By

Fig. 31 Stiffness–displacement curve of metastructure based on Eq. (25) for varying γ, when $\mu = 2$

Fig. 32 Stiffness–displacement curve of metastructure based on Eq. (25) for varying μ, when $\gamma = 0.5$

substituting these values of γ in Eq. (27), we can observe that

when $\gamma_{\min} = 0$, $\mu_{QZS} = 0$ and when $\gamma_{\max} = 1$, μ_{QZS}
$\qquad = $ undefined

$$(73)$$

Therefore, it can be seen that μ achieves singularity at $\gamma = 1$. The conditions shown in Eq. (73) are plotted in Fig. 33. It can be observed from the curve that for $\gamma_{\min} = 0$, the system behaves as an equivalent linear isolator with equivalent QZS equal to 8, and for $\gamma_{\max} = 1$, the value of equivalent QZS remains constant as zero throughout, which is practically difficult to achieve.

The limiting value obtained for γ can be used to find the limiting conditions for μ as well; Eq. (27) leads to

$$0 < \frac{\mu}{\mu + 2} < 1 \qquad (74)$$

From Eq. (74), it can be observed that

$$\mu > 0 \qquad (75)$$

As the stiffness cannot be negative, μ should always hold the condition mentioned in Eq. (75), and also $\mu \neq 0$, as it will lead the model to linear condition. A

stiffness–displacement curve (shown in Fig. 34) based on Eq. (25) is plotted for four different conditions of μ satisfying Eq. (27). It can be observed from the curve that $k_{QZS} = 0$ is achieved at static equilibrium position ($x = 0$) for all the four conditions of μ, therefore satisfying the QZS criterion.

Hence, it can be observed from the above discussions that the system is unstable for $\gamma < \gamma_{QZS}$ and $\mu > \mu_{QZS}$. The metastructure will hold the QZS property when $0 < \gamma < 1$ and $\mu > 0$. The singularity for μ is achieved when $\gamma_{QZS} = 1$.
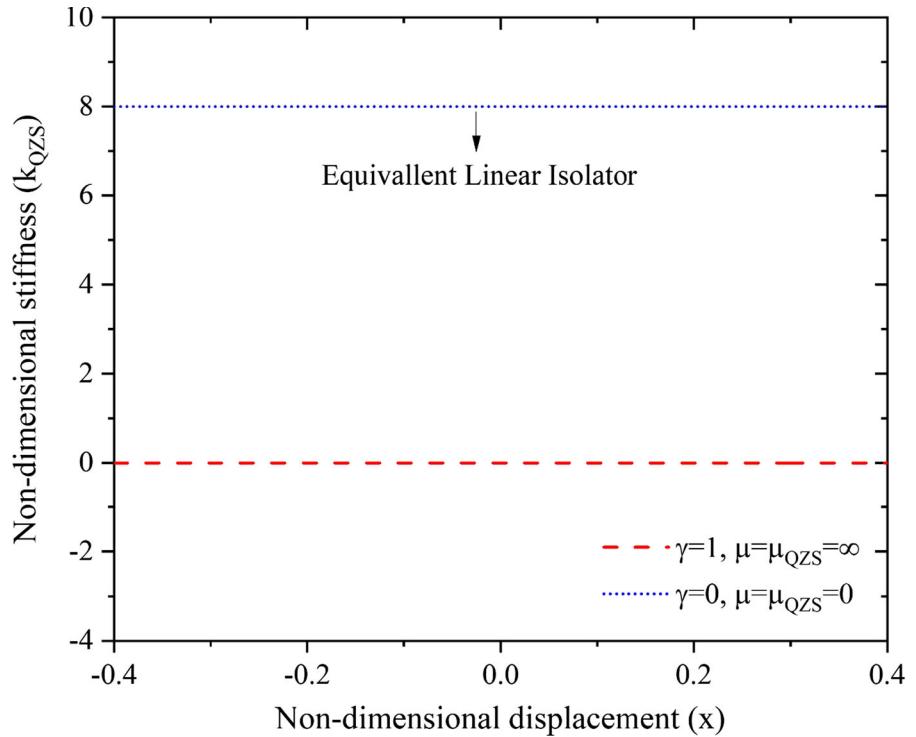
C. Derivation of Eq. (29)

$$k_{QZS}(x) = 8 + 4\mu - \frac{4\mu\gamma^2}{(\gamma^2 + x^2)^{3/2}} \qquad (25)$$
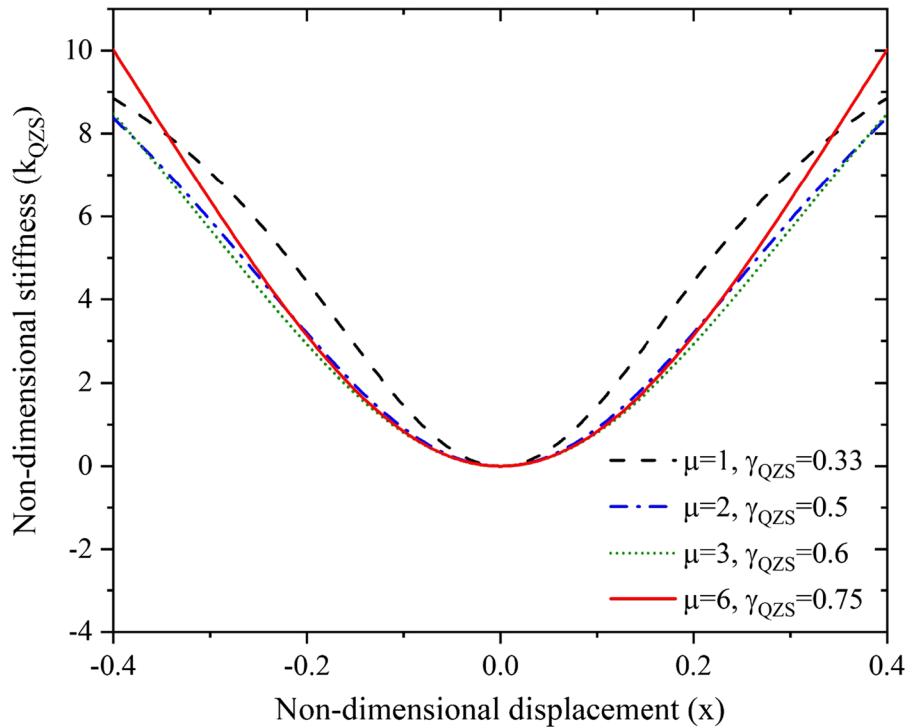
Satisfying the condition $k_{QZS}(x) < 8$ from Eq. (28) and substituting $\mu_{QZS} = \frac{2\gamma}{1-\gamma}$ from Eq. (27), Eq. (25) can be rewritten as

$$k_{QZS}(x) = 8 + 4\mu - \frac{4\mu\gamma^2}{(\gamma^2 + x^2)^{3/2}} < 8 \qquad (76)$$

Fig. 33 Stiffness–displacement curve of metastructure based on Eq. (25) plotted for two different conditions obtained from Eq. (73) i.e., (i) $\gamma_{min} = 0$ and (ii) $\gamma_{max} = 1$

Fig. 34 Stiffness–displacement curve of metastructure based on Eq. (25) plotted for four different conditions of μ satisfying Eq. (27)

$$8 + 4\left(\frac{2\gamma}{1-\gamma}\right) - \frac{4\left(\frac{2\gamma}{1-\gamma}\right)\gamma^2}{\left(\gamma^2 + x^2\right)^{3/2}} < 8 \tag{77}$$

$$4\left(\frac{2\gamma}{1-\gamma}\right) - \frac{4\left(\frac{2\gamma}{1-\gamma}\right)\gamma^2}{\left(\gamma^2 + x^2\right)^{3/2}} < 0 \tag{78}$$

$$1 - \frac{\gamma^2}{\left(\gamma^2 + x^2\right)^{3/2}} < 0 \tag{79}$$

$$\frac{\gamma^2}{\left(\gamma^2 + x^2\right)^{3/2}} > 1 \tag{80}$$

$$\left(\gamma^2 + x^2\right)^{3/2} < \gamma^2 \tag{81}$$

$$x^2 < \gamma^{4/3} - \gamma^2 \tag{82}$$

$$x^2 < \gamma^{4/3} - \gamma^{(4/3)+(2/3)} \tag{83}$$

$$x^2 < \gamma^{4/3}\left(1 - \gamma^{2/3}\right) \tag{84}$$

$$|x| < \gamma^{2/3}\sqrt{\left(1 - \gamma^{2/3}\right)}. \tag{29}$$

D. Derivation of Eq. (35)

From Eq. (34), Taylor series expansion is

$$f(x) = f(x_o) + \sum_{n=1}^{N} \frac{f^n(x_o)}{n!}(x - x_o)^n \tag{34}$$

Here,

$$f_{QZS}(x) = 8x - 4\mu\left(\frac{1}{\sqrt{\gamma^2 + x^2}} - 1\right)x \tag{24}$$

Finding the derivatives of $f(x_0)$

$$f(x_0) = 8x_0 - 4\mu\left(\frac{x_0}{\sqrt{\gamma^2 + x_0^2}} - x_0\right) \tag{85}$$

$$f'(x_0) = 8 + 4\mu - \frac{4\mu\gamma^2}{\left(\gamma^2 + x_0^2\right)^{3/2}} \tag{86}$$

$$f''(x_0) = \frac{12\mu x_0}{\left(\gamma^2 + x_0^2\right)^{3/2}} - \frac{12\mu x_0^3}{\left(\gamma^2 + x_0^2\right)^{5/2}} \tag{87}$$

$$f'''(x_0) = \frac{12\mu}{\left(\gamma^2 + x_0^2\right)^{3/2}} - \frac{72\mu x_0^2}{\left(\gamma^2 + x_0^2\right)^{5/2}} + \frac{60\mu x_0^4}{\left(\gamma^2 + x_0^2\right)^{7/2}} \tag{88}$$

$$f^{iv}(x_0) = \frac{600\mu x_0^3}{\left(\gamma^2 + x_0^2\right)^{7/2}} - \frac{420\mu x_0^5}{\left(\gamma^2 + x_0^2\right)^{9/2}} - \frac{180\mu x_0}{\left(\gamma^2 + x_0^2\right)^{5/2}} \tag{89}$$

$$f^{v}(x_0) = \frac{2700\mu x_0^2}{\left(\gamma^2 + x_0^2\right)^{7/2}} - \frac{180\mu}{\left(\gamma^2 + x_0^2\right)^{5/2}} - \frac{6300\mu x_0^4}{\left(\gamma^2 + x_0^2\right)^{9/2}} + \frac{3780\mu x_0^6}{\left(\gamma^2 + x_0^2\right)^{11/2}} \tag{90}$$

$$f^{vi}(x_0) = \frac{79380\mu x_0^5}{\left(\gamma^2 + x_0^2\right)^{11/2}} - \frac{44100\mu x_0^3}{\left(\gamma^2 + x_0^2\right)^{9/2}} - \frac{41580\mu x_0^7}{\left(\gamma^2 + x_0^2\right)^{13/2}} + \frac{6300\mu x_0}{\left(\gamma^2 + x_0^2\right)^{7/2}} \tag{91}$$

$$f^{vii}(x_0) = \frac{6300\mu}{\left(\gamma^2 + x_0^2\right)^{7/2}} - \frac{176400\mu x_0^2}{\left(\gamma^2 + x_0^2\right)^{9/2}} + \frac{793800\mu x_0^4}{\left(\gamma^2 + x_0^2\right)^{11/2}} - \frac{1164240\mu x_0^6}{\left(\gamma^2 + x_0^2\right)^{13/2}} + \frac{540540\mu x_0^8}{\left(\gamma^2 + x_0^2\right)^{15/2}} \tag{92}$$

Substituting $x_0 = 0$ in Eq. (92),

$$f(0) = 0 \quad f'(0) = 8 + 4\mu\left(1 - \frac{1}{\gamma}\right) \quad f''(0) = 0$$
$$f'''(0) = \frac{12\mu}{\gamma^3} \tag{93}$$

$$f^{iv}(0) = 0 \quad f^{v}(0) = -\frac{180\mu}{\gamma^5} \quad f^{vi}(0) = 0$$
$$f^{vii}(0) = -\frac{6300\mu}{\gamma^7} \tag{94}$$

By expanding Eq. (24) using Eq. (34), the expression for the force–displacement can be approximated as Eq. (35):

$$f(x) = \left[8 + 4\mu\left(\frac{\gamma - 1}{\gamma}\right)\right]x + \frac{2\mu}{\gamma^3}x^3 - \frac{3\mu}{2\gamma^5}x^5 + \frac{5\mu}{4\gamma^7}x^7. \tag{35}$$

E. Derivation of Eq. (49)

First representing Eq. (47a) and (47b)

$$-\Omega^2 A + \left(\frac{3}{4}\alpha A^3\right) + \left(\frac{5}{8}\delta A^5\right) = -z_0\cos(\phi) \quad (47a)$$

$$-2\xi A\Omega = -z_0\sin(\phi) \quad (47b)$$

Squaring and adding Eq. (47a) and (47b), and thereafter eliminating ϕ,

$$\Omega^4 A^2 + \frac{9}{16}\alpha^2 A^6 + \frac{25}{64}\delta^2 A^{10} - \frac{3}{2}\Omega^2\alpha A^4 - \frac{5}{4}\Omega^2\delta A^6$$
$$+ \frac{15}{16}\delta\alpha A^8 + 4\xi^2\Omega^2 A^2$$
$$= z_0^2$$

$$(95)$$

$$\Omega^4 A^2 + \Omega^2\left[4\xi^2 A^2 - \frac{3}{2}\alpha A^4 - \frac{5}{4}\delta A^6\right]$$
$$+ \left[\frac{9}{16}\alpha^2 A^6 + \frac{25}{64}\delta^2 A^{10}\frac{15}{16}\delta\alpha A^8 - z_0^2\right]$$
$$= 0 \quad (96)$$

Let, $\Omega^2 = w$

$$w^2 A^2 + w\left[4\xi^2 A^2 - \frac{3}{2}\alpha A^4 - \frac{5}{4}\delta A^6\right]$$
$$+ \left[\frac{9}{16}\alpha^2 A^6 + \frac{25}{64}\delta^2 A^{10}\frac{15}{16}\delta\alpha A^8 - z_0^2\right]$$
$$= 0 \quad (97)$$

$$w = -\frac{b}{2a} \pm \frac{\sqrt{b^2 - 4ac}}{2a} \quad (98)$$

$$w = \left(-2\xi^2 + \frac{3}{4}\alpha A^2 + \frac{5}{8}\delta A^4\right)$$
$$\pm \sqrt{\left(2\xi^2 - \frac{3}{4}\alpha A^2 - \frac{5}{8}\delta A^4\right)^2 - \left(\frac{9}{16}\alpha^2 A^4 + \frac{25}{64}\delta^2 A^8 + \frac{15}{16}\delta\alpha A^6 - \frac{z_0^2}{A^2}\right)}$$
$$(99)$$

Substituting, $w = \Omega^2$

$$\Omega = \pm\left\{\left(\frac{3}{4}\alpha A^2 + \frac{5}{8}\delta A^4 - 2\xi^2\right)\right.$$
$$\pm\left[\left(-\frac{3}{4}\alpha A^2 - \frac{5}{8}\delta A^4 + 2\xi^2\right)^2\right.$$
$$\left.\left.- \left(\frac{9}{16}\alpha^2 A^4 + \frac{25}{64}\delta^2 A^8 + \frac{15}{16}\delta\alpha A^6 - \frac{z_0^2}{A^2}\right)\right]^{1/2}\right\}^{1/2}.$$
$$(49)$$

F. Derivation of Eqs. (50), (51), (52), and (53)

At the peak resonance point, both the intersections coincide with each other, i.e., Ω_1 became equal to Ω_2 of Eq. (49).

Considering only the real part, Ω_1 and Ω_2 can be written as

$$\Omega_1 = \left\{\left(\frac{3}{4}\alpha A^2 + \frac{5}{8}\delta A^4 - 2\xi^2\right)\right.$$
$$+ \left[\left(-\frac{3}{4}\alpha A^2 - \frac{5}{8}\delta A^4 + 2\xi^2\right)^2\right.$$
$$\left.\left.- \left(\frac{9}{16}\alpha^2 A^4 + \frac{25}{64}\delta^2 A^8 + \frac{15}{16}\delta\alpha A^6 - \frac{z_0^2}{A^2}\right)\right]^{1/2}\right\}^{1/2}$$
$$(49a)$$

$$\Omega_2 = \left\{\left(\frac{3}{4}\alpha A^2 + \frac{5}{8}\delta A^4 - 2\xi^2\right)\right.$$
$$- \left[\left(-\frac{3}{4}\alpha A^2 - \frac{5}{8}\delta A^4 + 2\xi^2\right)^2\right.$$
$$\left.\left.- \left(\frac{9}{16}\alpha^2 A^4 + \frac{25}{64}\delta^2 A^8 + \frac{15}{16}\delta\alpha A^6 - \frac{z_0^2}{A^2}\right)\right]^{1/2}\right\}^{1/2}$$
$$(49b)$$

Equating Eq. (49a) and (49b),

$$2\left[\left(-\frac{3}{4}\alpha A^2 - \frac{5}{8}\delta A^4 + 2\xi^2\right)^2\right.$$
$$\left.- \left(\frac{9}{16}\alpha^2 A^4 + \frac{25}{64}\delta^2 A^8 + \frac{15}{16}\delta\alpha A^6 - \frac{z_0^2}{A^2}\right)\right]^{1/2}$$
$$= 0$$
$$(100)$$

$$\frac{9}{16}\alpha^2 A^4 + \frac{25}{64}\delta^2 A^8 + 4\xi^4 + \frac{15}{16}\delta\alpha A^6 - 3\alpha A^2 \xi^2$$
$$- \frac{5}{2}\delta A^4 \xi^2 - \frac{9}{16}\alpha^2 A^4 - \frac{25}{64}\delta^2 A^8 - \frac{15}{16}\delta\alpha A^6 + \frac{z_0^2}{A^2}$$
$$= 0 \tag{101}$$

$$4\xi^4 - 3\alpha A^2 \xi^2 - \frac{5}{2}\delta A^4 \xi^2 + \frac{z_0^2}{A^2} = 0 \tag{102}$$

$$3\alpha A^4 + \frac{5}{2}\delta A^6 - 4\xi^2 A^2 - \frac{z_0^2}{\xi^2} = 0 \tag{103}$$

Denoting A as peak amplitude (A_p)

$$\frac{5}{2}\delta A_p^6 + 3\alpha A_p^4 - 4\xi^2 A_p^2 - \frac{z_0^2}{\xi^2} = 0 \tag{50}$$

At this peak resonance, peak frequency (Ω_p) occurs, using Eq. (49) to derive the relation of Ω_p. As it is clear that, at resonance condition, the nested square root of Eq. (49) is zero, so Ω_p can be calculated as

$$\Omega_1 = \left\{ \left(\frac{3}{4}\alpha A_p^2 + \frac{5}{8}\delta A_p^4 - 2\xi^2 \right) + 0 \right\}^{1/2} \tag{104}$$

$$\Omega_2 = \left\{ \left(\frac{3}{4}\alpha A_p^2 + \frac{5}{8}\delta A_p^4 - 2\xi^2 \right) + 0 \right\}^{1/2} \tag{105}$$

$$\Omega_p = \sqrt{\frac{3}{4}\alpha A_p^2 + \frac{5}{8}\delta A_p^4 - 2\xi^2} \tag{51}$$

Equating Eq. (51) to zero,

$$\Omega_p = \sqrt{\frac{3}{4}\alpha A_p^2 + \frac{5}{8}\delta A_p^4 - 2\xi^2} = 0 \tag{106}$$

$$\frac{5}{8}\delta A_p^4 + \frac{3}{4}\alpha A_p^2 - 2\xi^2 = 0 \tag{107}$$

$$\frac{5}{8}\delta \left(A_p^2 \right)^2 + \frac{3}{4}\alpha \left(A_p^2 \right) - 2\xi^2 = 0 \tag{108}$$

$$A_p^2 = \frac{\left(-\frac{3}{4}\alpha \right) \pm \sqrt{\left(\frac{3}{4}\alpha \right)^2 + 5\delta\xi^2}}{\frac{5}{4}\delta} \tag{109}$$

$$A_p^2 = \frac{1}{\delta} \left(\sqrt{\frac{9}{25}\alpha^2 + \frac{16}{5}\delta\xi^2} - \frac{3}{5}\alpha \right) \tag{52}$$

Substituting Eq. (52) into Eq. (50) and ignoring the higher-order amplitude term,

$$z_0^2 = 4\xi^4 \frac{1}{\delta} \left(\sqrt{\frac{9}{25}\alpha^2 + \frac{16}{5}\delta\xi^2} - \frac{3}{5}\alpha \right) \tag{110}$$

$$z_0 = 2\xi^2 \sqrt{\frac{1}{\delta} \left(\sqrt{\frac{9}{25}\alpha^2 + \frac{16}{5}\delta\xi^2} - \frac{3\alpha}{5\delta} \right)}. \tag{53}$$

G. Derivation of Eqs. (55) and (56)

Considering Eq. (54),

$$T = \frac{\sqrt{(\Omega^4 A^2) - (2\Omega^2 A z_0 \cos\phi) + z_0^2}}{z_0} \tag{54}$$

Finding out the value of $\cos(\phi)$ form Eq. (47a), and substituting in Eq. (54),

$$\cos(\phi) = -\frac{-\Omega^2 A + \left(\frac{3}{4}\alpha A^3 \right) + \left(\frac{5}{8}\delta A^5 \right)}{z_0} \tag{111}$$

$$T = \frac{\sqrt{(\Omega^4 A^2) - (2\Omega^2 A z_0 \cos\phi) + z_0^2}}{z_0} \tag{112}$$

$$T = \frac{\sqrt{(\Omega^4 A^2) + \left(-2\Omega^4 A^2 + \left(\frac{3}{2}\Omega^2 \alpha A^4 \right) + \left(\frac{5}{4}\Omega^2 \delta A^6 \right) \right) + z_0^2}}{z_0} \tag{113}$$

$$T = \sqrt{-\frac{\Omega^4 A^2}{z_0^2} + \frac{\frac{3}{2}\Omega^2 \alpha A^4}{z_0^2} + \frac{\frac{5}{4}\Omega^2 \delta A^6}{z_0^2} + 1} \tag{114}$$

$$T = \sqrt{\left(\frac{\Omega A}{z_0} \right)^2 \left(\frac{5}{4}\delta A^4 + \frac{3}{2}\alpha A^2 - \Omega^2 \right) + 1} \tag{55}$$

By substituting the value of Ω as Ω_p from Eq. (50) and A as A_p, the value of peak transmissibility T_p can be obtained:

$$\Omega = \Omega_p = \sqrt{\frac{3}{4}\alpha A_p^2 + \frac{5}{8}\delta A_p^4 - 2\xi^2} \tag{115}$$

$$A^2 = A_p^2 = \frac{1}{\delta} \left(\sqrt{\frac{9}{25}\alpha^2 + \frac{16}{5}\delta\xi^2} - \frac{3}{5}\alpha \right) \tag{116}$$

$$T_p = \sqrt{\frac{A_p^2}{z_0^2} \left[\left(\frac{5}{8}\delta A_p^2 + \frac{3}{4}\alpha \right)^2 A_p^4 - 4\xi^4 \right] + 1}. \tag{56}$$

H. Derivation of Eqs. (59), (61), and (62)

Substituting Eq. (58) into Eq. (43),

$$y(\tau) = A\cos(\Omega\tau + \phi) + \varepsilon(\tau) \tag{58}$$

$$y'' + 2\xi y' + \alpha y^3 + \delta y^5 = -z_0\cos(\Omega\tau) \tag{43}$$

Finding out the value of variables,

$$\Omega\tau + \phi = \theta \tag{117}$$

$$-z_0\cos(\Omega\tau) = -z_0\cos\theta\cos\phi - z_0\sin\theta\sin\phi \tag{118}$$

$$y(\tau) = A\cos(\Omega\tau + \phi) + \varepsilon(\tau) \tag{119}$$

$$y'(\tau) = -A\Omega\sin\theta + \varepsilon'(\tau) \tag{120}$$

$$y'' = -A\Omega^2\cos\theta + \varepsilon''(\tau) \tag{121}$$

Ignoring the term of order higher than $O(\varepsilon^2)$, and also assuming a harmonic response,

$$y^3 = \left(A^3\cos^3\theta + 3\varepsilon A^2\cos^2\theta\right) \tag{122}$$

$$\cos^3\theta = \frac{3}{4}\cos\theta \tag{123}$$

$$\cos^2\theta = \frac{\cos 2\theta + 1}{2} \tag{124}$$

$$y^3 = \left(A^3\frac{3}{4}\cos\theta + 3\varepsilon A^2\frac{\cos 2\theta + 1}{2}\right) \tag{125}$$

Substituting all these values into Eq. (43), and performing the first-order perturbation analysis by ignoring the term of order higher than $O(\epsilon^2)$, and also assuming a harmonic response, the equation of motion can be expressed in the form of

$$\varepsilon'' + 2\mu\varepsilon' + (p - 2q\cos 2\theta)\varepsilon = 0 \tag{59}$$

Here,

$$p = \frac{3\alpha A^2}{2\Omega^2}, \quad q = -\frac{3\alpha A^2}{4\Omega^2}, \quad \mu = \frac{\xi}{\Omega} \tag{60}$$

The solution of Eq. (59) is unstable if it lies outside the parabola:

$$p = 1 \pm \sqrt{q^2 - 4\mu^2} \tag{61}$$

By substituting Eq. (60) into Eq. (61),

$$\frac{3\alpha A^2}{2\Omega^2} = 1 \pm \sqrt{\left(-\frac{3\alpha A^2}{4\Omega^2}\right)^2 - 4\left(\frac{\xi}{\Omega}\right)^2} \tag{126}$$

$$3\alpha A^2 = 2\Omega^2 \pm \sqrt{\left(\frac{9\alpha^2 A^4}{4}\right) - 16\xi^2\Omega^2} \tag{127}$$

$$3\alpha A^2 - 2\Omega^2 = \pm\sqrt{\left(\frac{9\alpha^2 A^4}{4}\right) - 16\xi^2\Omega^2} \tag{128}$$

$$9\alpha^2 A^4 + 4\Omega^4 - 12\alpha A^2\Omega^2 = \frac{9\alpha^2 A^4}{4} - 16\xi^2\Omega^2 \tag{129}$$

$$4\Omega^4 + \frac{27\alpha^2 A^4}{4} + \Omega^2\left(16\xi^2 - 12\alpha A^2\right) = 0 \tag{130}$$

$$\Omega^4 + \Omega^2\left(4\xi^2 - 3\alpha A^2\right) + \frac{27\alpha^2 A^4}{16} = 0 \tag{131}$$

$$\Omega_{\text{us1}} = \sqrt{\frac{3}{2}\alpha A^2 - 2\xi^2 + \frac{1}{2}\sqrt{\left(4\xi^2 - 3\alpha A^2\right)^2 - \frac{27}{4}\alpha^2 A^4}} \tag{62a}$$

$$\Omega_{\text{us2}} = \sqrt{\frac{3}{2}\alpha A^2 - 2\xi^2 - \frac{1}{2}\sqrt{\left(4\xi^2 - 3\alpha A^2\right)^2 - \frac{27}{4}\alpha^2 A^4}}. \tag{62b}$$

References

1. Allan, G.P., Thomas, L.P.: Harris' Shock and Vibration Handbook, 6th edn. McGraw-Hill Education, New York (2010)
2. Wei, X., Zhu, M., Jia, L.: A semi-active control suspension system for railway vehicles with magnetorheological fluid dampers. Veh. Syst. Dyn. **54**(7), 982–1003 (2016)
3. Dalela, S., Balaji, P.S., Jena, D.P.: A review on application of mechanical metamaterials for vibration control. Mech. Adv. Mater. Struct. (2021). https://doi.org/10.1080/15376494.2021.1892244
4. Wang, X., Yao, H., Zheng, G.: Enhancing the isolation performance by a nonlinear secondary spring in the Zener model. Nonlinear Dyn. **87**(4), 2483–2495 (2017)
5. Huang, X., et al.: The isolation performance of vibration systems with general velocity-displacement-dependent nonlinear damping under base excitation: numerical and experimental study. Nonlinear Dyn. **85**(2), 777–796 (2016)
6. Zeqi, L., Liqun, C.: Some recent progresses in nonlinear passive isolations of vibrations. Chin. J. Theor. Appl. Mech. **49**(3), 550 (2017)

7. Balaji, P.S., Karthik SelvaKumar, K.: Applications of nonlinearity in passive vibration control: a review. J. Vib. Eng. Technol. **9**(2), 183–213 (2021)

8. Wang, K., et al.: Low-frequency band gaps in a metamaterial rod by negative-stiffness mechanisms: design and experimental validation. Appl. Phys. Lett. **114**(25), 251902 (2019)

9. Antoniadis, I., et al.: Hyper-damping properties of a stiff and stable linear oscillator with a negative stiffness element. J. Sound Vib. **346**, 37–52 (2015)

10. Carrella, A., Brennan, M., Waters, T.: Static analysis of a passive vibration isolator with quasi-zero-stiffness characteristic. J. Sound Vib. **301**(3–5), 678–689 (2007)

11. Tang, B., Brennan, M.: On the shock performance of a nonlinear vibration isolator with high-static-low-dynamic-stiffness. Int. J. Mech. Sci. **81**, 207–214 (2014)

12. Lan, C.-C., Yang, S.-A., Wu, Y.-S.: Design and experiment of a compact quasi-zero-stiffness isolator capable of a wide range of loads. J. Sound Vib. **333**(20), 4843–4858 (2014)

13. Ahn, H.-J.: Performance limit of a passive vertical isolator using a negative stiffness mechanism. J. Mech. Sci. Technol. **22**(12), 2357 (2008)

14. Carrella, A., Brennan, M., Waters, T.: Optimization of a quasi-zero-stiffness isolator. J. Mech. Sci. Technol. **21**(6), 946–949 (2007)

15. Carrella, A., et al.: On the force transmissibility of a vibration isolator with quasi-zero-stiffness. J. Sound Vib. **322**(4–5), 707–717 (2009)

16. Carrella, A., et al.: Force and displacement transmissibility of a nonlinear isolator with high-static-low-dynamic-stiffness. Int. J. Mech. Sci. **55**(1), 22–29 (2012)

17. Kovacic, I., Brennan, M.J., Waters, T.P.: A study of a nonlinear vibration isolator with a quasi-zero stiffness characteristic. J. Sound Vib. **315**(3), 700–711 (2008)

18. Ledezma-Ramirez, D.F., et al.: An experimental nonlinear low dynamic stiffness device for shock isolation. J. Sound Vib. **347**, 1–13 (2015)

19. Liu, C., Yu, K.: Accurate modeling and analysis of a typical nonlinear vibration isolator with quasi-zero stiffness. Nonlinear Dyn. **100**(3), 2141–2165 (2020)

20. Fulcher, B.A., et al.: Analytical and experimental investigation of buckled beams as negative stiffness elements for passive vibration and shock isolation systems. J. Vib. Acoust. **136**(3), 031009 (2014)

21. Huang, X., et al.: Vibration isolation characteristics of a nonlinear isolator using Euler buckled beam as negative stiffness corrector: a theoretical and experimental study. J. Sound Vib. **333**(4), 1132–1148 (2014)

22. Huang, X., et al.: Shock isolation performance of a nonlinear isolator using Euler buckled beam as negative stiffness corrector: theoretical and experimental study. J. Sound Vib. **345**, 178–196 (2015)

23. Liu, X., Huang, X., Hua, H.: On the characteristics of a quasi-zero stiffness isolator using Euler buckled beam as negative stiffness corrector. J. Sound Vib. **332**(14), 3359–3376 (2013)

24. Zheng, Y., et al.: Analytical study of a quasi-zero stiffness coupling using a torsion magnetic spring with negative stiffness. Mech. Syst. Signal Process. **100**, 135–151 (2018)

25. Dong, G., et al.: Simulated and experimental studies on a high-static-low-dynamic stiffness isolator using magnetic negative stiffness spring. Mech. Syst. Signal Process. **86**, 188–203 (2017)

26. Jing, X., et al.: A novel bio-inspired anti-vibration structure for operating hand-held jackhammers. Mech. Syst. Signal Process. **118**, 317–339 (2019)

27. Ishida, S., Suzuki, K., Shimosaka, H.: Design and experimental analysis of origami-inspired vibration isolator with quasi-zero-stiffness characteristic. J. Vib. Acoust. **139**(5), 051004 (2017)

28. Vakakis, A.F.: Inducing passive nonlinear energy sinks in vibrating systems. J. Vib. Acoust. **123**(3), 324–332 (2001)

29. Zhou, J., et al.: Local resonator with high-static-low-dynamic stiffness for lowering band gaps of flexural wave in beams. J. Appl. Phys. **121**(4), 044902 (2017)

30. Wang, K., et al.: Mathematical modeling and analysis of a meta-plate for very low-frequency band gap. Appl. Math. Model. **73**, 581–597 (2019)

31. Wen, G., et al.: Design, analysis and semi-active control of a quasi-zero stiffness vibration isolation system with six oblique springs. Nonlinear Dyn. **106**, 309–321 (2021)

32. Han, W.-J., et al.: A high-static-low-dynamics stiffness vibration isolator via an elliptical ring. Mech. Syst. Signal Process. **162**, 108061 (2022)

33. Che, K., et al.: Three-dimensional-printed multistable mechanical metamaterials with a deterministic deformation sequence. J. Appl. Mech. **84**(1), 011004 (2017)

34. Ren, C., Yang, D., Qin, H.: Mechanical performance of multidirectional buckling-based negative stiffness metamaterials: an analytical and numerical study. Materials **11**(7), 1078 (2018)

35. Izard, A.G., et al.: Optimal design of a cellular material encompassing negative stiffness elements for unique combinations of stiffness and elastic hysteresis. Mater. Des. **135**, 37–50 (2017)

36. Tan, X., et al.: Reusable metamaterial via inelastic instability for energy absorption. Int. J. Mech. Sci. **155**, 509–517 (2019)

37. Ha, C.S., Lakes, R.S., Plesha, M.E.: Design, fabrication, and analysis of lattice exhibiting energy absorption via snap-through behavior. Mater. Des. **141**, 426–437 (2018)

38. Tan, X., et al.: A novel cylindrical negative stiffness structure for shock isolation. Compos. Struct. **214**, 397–405 (2019)

39. Yang, H., Ma, L.: Multi-stable mechanical metamaterials with shape-reconfiguration and zero Poisson's ratio. Mater. Des. **152**, 181–190 (2018)

40. Frenzel, T., et al.: Tailored buckling microlattices as reusable light-weight shock absorbers. Adv. Mater. **28**(28), 5865–5870 (2016)

41. Peng, Z.K., et al.: Study of the effects of cubic nonlinear damping on vibration isolations using harmonic balance method. Int. J. Nonlinear Mech. **47**(10), 1073–1080 (2012)

42. Qiu, J., Lang, J.H., Slocum, A.H.: A curved-beam bistable mechanism. J. Microelectromech. Syst. **13**(2), 137–146 (2004)

43. Vangbo, M.: An analytical analysis of a compressed bistable buckled beam. Sens. Actuators A **69**(3), 212–216 (1998)

44. Fan, H., et al.: Design of metastructures with quasi-zero dynamic stiffness for vibration isolation. Compos. Struct. **243**, 112244 (2020)

45. Brennan, M., et al.: On the jump-up and jump-down frequencies of the Duffing oscillator. J. Sound Vib. **318**(4–5), 1250–1261 (2008)

46. Hamdan, M.N., Burton, T.D.: On the steady state response and stability of nonlinear oscillators using harmonic balance. J. Sound Vib. **166**(2), 255–266 (1993)

47. Worden, K.: Nonlinearity in Structural Dynamics: Detection, Identification and Modelling. CRC Press, New York (2019)

48. Ravindra, B., Mallik, A.K.: Performance of nonlinear vibration isolators under harmonic excitation. J. Sound Vib. **170**(3), 325–337 (1994)

49. Taylor, J.H., Narendra, K.S.: Stability regions for the damped Mathieu equation. SIAM J. Appl. Math. **17**(2), 343–352 (1969)

50. Nayfeh, A.H., Mook, D.T., Holmes, P.: Nonlinear Oscillations. Wiley, New York (1980)